

Mapping surface deformation and thermal dilation of arch bridges by structure-driven multi-temporal DInSAR analysis

Qin, Xiaoqiong; Zhang, Lu; Yang, Mengshi; Luo, Heng; Liao, Mingsheng; Ding, Xiaoli

DOI

[10.1016/j.rse.2018.06.032](https://doi.org/10.1016/j.rse.2018.06.032)

Publication date

2018

Document Version

Final published version

Published in

Remote Sensing of Environment

Citation (APA)

Qin, X., Zhang, L., Yang, M., Luo, H., Liao, M., & Ding, X. (2018). Mapping surface deformation and thermal dilation of arch bridges by structure-driven multi-temporal DInSAR analysis. *Remote Sensing of Environment*, 216, 71-90. <https://doi.org/10.1016/j.rse.2018.06.032>

Important note

To cite this publication, please use the final published version (if applicable). Please check the document version above.

Copyright

Other than for strictly personal use, it is not permitted to download, forward or distribute the text or part of it, without the consent of the author(s) and/or copyright holder(s), unless the work is under an open content license such as Creative Commons.

Takedown policy

Please contact us and provide details if you believe this document breaches copyrights. We will remove access to the work immediately and investigate your claim.

Green Open Access added to TU Delft Institutional Repository

'You share, we take care!' - Taverne project

<https://www.openaccess.nl/en/you-share-we-take-care>

Otherwise as indicated in the copyright section: the publisher is the copyright holder of this work and the author uses the Dutch legislation to make this work public.



Mapping surface deformation and thermal dilation of arch bridges by structure-driven multi-temporal DInSAR analysis

Xiaoqiong Qin^{a,b}, Lu Zhang^a, Mengshi Yang^{a,c}, Heng Luo^a, Mingsheng Liao^{a,d,*}, Xiaoli Ding^b

^a State Key Laboratory of Information Engineering in Surveying, Mapping and Remote Sensing, Wuhan University, Wuhan 430079, China

^b Department of Land Surveying and Geo-Informatics, The Hong Kong Polytechnic University, Kowloon, Hong Kong, China

^c Department of Geoscience and Remote Sensing, Delft University of Technology, Delft 2628CN, the Netherlands

^d Key Laboratory of Land Subsidence Monitoring and Prevention, Ministry of Land and Resources, Shanghai 200072, China

ARTICLE INFO

Keywords:

Arch bridges
Structural Health Monitoring (SHM)
Thermal dilation
Deformation Feature Points
synthetic aperture radar interferometry (InSAR)
Time-series analysis

ABSTRACT

Arch bridges are important transportation infrastructures widely distributed in China, but they are prone to structural defects due to aging without routine inspection and maintenance. Therefore, Structural Health Monitoring (SHM) of these bridges is urgently needed by civil engineers to effectively reduce the risk of bridge damage or collapse on public safety. An essential method for SHM, the modern Differential Synthetic Aperture Radar Interferometry (DInSAR) technique, can detect subtle deformation of bridges at relatively low costs. Nevertheless, identifying dense point-like targets (PTs) on such partially coherent arch bridges in SAR image is more difficult than that for other man-made objects, owing to their complex structures and backscattering behaviors. Furthermore, the complex mechanical properties of arch bridges, due to the varying arch-beam interactions, make it hard to separate the surface deformation and thermal dilation accurately, and the lack of specific structural knowledge, that can help to understand the deformation evolution process, limits the global structural risk assessment. Aiming at these problems, we developed a structure-driven multi-temporal DInSAR approach for arch bridge-specific SHM. By introducing three structure-driven steps, i.e. backscattering geometrical interpretation, linear thermal dilation estimation and validation, and Deformation Feature Points (DFPs) based risk assessment, into the traditional DInSAR method, the reliability of PTs identification, thermal dilation separation, and structural risk assessment for arch bridges are significantly improved. The effectiveness of our approach was fairly presented by two case studies of the Rainbow and Lupu bridges, and the experimental results were verified by leveling benchmark validation, cross-sensor comparison, as well as structural-reliability assessment. Our results revealed that arch bridges exhibit a similar pattern of PTs distribution that is dense around piers and sparse on the spans, as well as a symmetrical progressive pattern of surface deformation with the subsidence increasing from piers and reaching a peak at the central spans. In contrast, magnitudes and mechanisms of thermal dilation are different, and highly dependent on the materials and structural characteristics of specific bridges.

1. Introduction

Arch bridges are widely used for connecting public transportation in populated cities, due to their attractive appearance and easy construction (Li et al., 2012). Acting as economic lifelines, the collapse of these bridges would cause huge financial and human losses (Ahlborn et al., 2010; Ismail et al., 2012; Sousa and Bastos, 2013). According to statistics, more than 100 bridge collapse accidents occurred in China since 2000 due to the lack of safety monitoring, resulting in substantial property damage and serious human casualties (Ji and Fu, 2010). Therefore, Structural Health Monitoring (SHM) of bridges has been

deeply recognized as a vital measure to gain up-to-date information on their structural safety, so as to detect the early warnings of damages or collapses and to reduce the potential threats on public safety.

Traditional bridge SHM relies largely on in-situ measurements by sensors such as the total stations, accelerometers, strain meters, and even visual inspections (Beshr, 2015). However, such measurements are generally available only at sparse discrete locations or with low temporal sampling frequency due to constraints on manpower and financial costs (Yi et al., 2010; Beshr and Kaloop, 2013). Moreover, these in-situ sensors, working continuously in harsh environments, are vulnerable to damage and difficult to repair, leading to reduced performance and

* Corresponding author at: No. 129 Luoyu Road, Wuhan, China.

E-mail addresses: qinxiaoqiong@whu.edu.cn (X. Qin), liao@whu.edu.cn (M. Liao).

shorter life expectancy (Ahlborn et al., 2010; Beshr, 2015). Consequently, the high-resolution, low-cost, and long-term routine SHM of bridges often proved to be an engineering challenge by using traditional measurement techniques, and thus innovative technologies are urgently required.

The Differential Synthetic Aperture Radar Interferometry (DInSAR) technology has been established as a powerful geodetic tool applied in various fields of earth science and engineering (Teatini et al., 2005; Vilardo et al., 2009; Zhang et al., 2012; Lan et al., 2012; Zhao et al., 2015). This non-contact technique outperforms the conventional survey methods due to the unique advantages of intensive detectable measurements, high monitoring precision, and routine inspection capacity without installing equipment or accessing the study area (Chang and Hanssen, 2014; Shamshiri et al., 2014; Milillo et al., 2016). However, effects of spatial/temporal de-correlation and atmospheric disturbances in conventional DInSAR analyses often restrict the robust estimation of reliable deformation parameters. Accordingly, the multi-temporal DInSAR techniques, combining Persistent Scatterers Interferometry (PSI) and Small Baseline (SBAS), have been developed to suppress the noise resulting from decorrelation and atmosphere bias by investigating the deformation of point-like targets (PTs) (Ferretti et al., 2001; Berardino et al., 2002; Casu et al., 2006; Hooper, 2008; Qu et al., 2015; Osmanoglu et al., 2016). The existing methods however, are especially suitable for the large-scale ground subsidence detecting by using early medium-resolution SAR images, rather than aiming at the detailed monitoring for bridges based on high-resolution SAR images. Therefore, few pioneer works have been conducted to investigate the accuracy and sensitivity of DInSAR-based deformation measurements on bridges until the operation of high-resolution X-band SAR sensors (Fornaro et al., 2013; Sousa and Bastos, 2013; Huang et al., 2017; Lazecky et al., 2017).

However, the deformation monitoring of bridges is still difficult because the signal processing and interpretation for these complex structures that change with time in SAR images remain significant challenges to overcome (Soergel et al., 2008; Invernizzi et al., 2011). We argue that those studies previously published on bridge monitoring with SAR data are insufficient because most of them focused either on girder bridges over land or bridges of extremely large-scales, neglecting the widespread medium-sized arch bridges upon which various deformation patterns also exist. Normally, girder bridges are totally coherent structures exhibiting mainly single-bounce signals in SAR images, making it easy to identify intensive PTs with the conventional DInSAR method (Fornaro et al., 2013; Lazecky et al., 2014, 2017). Large-scale bridges, on the other hand, are not common in daily life and usually have excellent basic conditions and timely post-maintenance, resulting in a less urgent requirement for deformation monitoring (Wong, 2004; Chen et al., 2011; Huang et al., 2017).

The widely distributed arch bridges however, are not subject to routine monitoring and easy to suffer from structural defects (Invernizzi et al., 2011). Hence, monitoring arch bridges is of utmost significant to prevent public death and injuries. Nevertheless, most arch bridges are partially coherent in SAR images due to their complex structures and backscattering behaviors, making it more difficult to identify a large number of PTs compared with other types of bridges, and thus more urgent to develop new methods. Furthermore, surface deformation and thermal dilation of arch bridges are often mixed together due to the arch-beam interactions, requiring reliable methods to accurately estimate and validate the thermal dilation. Additionally, lacking of specific structural knowledge, including geolocation, material, and mechanical properties, that can help to understand the deformation evolution process, it is hard to achieve a reliable global structural risk assessment on the bridge with only InSAR measurements.

To address these issues, a structure-driven multi-temporal DInSAR approach for arch bridge-specific SHM was developed in this study. By considering the structural properties of arch bridges, three structure-driven improvements, i.e. backscattering geometrical interpretation, linear thermal dilation estimation and validation, and Deformation

Feature Points (DFPs) based risk assessment, were implemented in our approach to improve the reliability of PTs identification, thermal dilation separation, and structural risk assessment. The method integrated the coherent and incoherent information of SAR images, the structural knowledge of bridges, as well as the temperature records into the data processing and results interpretation, and was tested by two case studies of the Rainbow and Lupu bridges using X-band and C-band SAR data. The experimental results were at millimeter-level accuracy according to the validation with leveling data, cross-sensor measurements, and structural-reliability principle. Our results demonstrated that the PTs selected on arch bridges, exhibit a similar distribution pattern which is intensive near the piers and sparse on the spans. Moreover, a symmetrical progressive pattern of surface deformation, with the subsidence increasing from piers and reaching a peak in the middle of spans, is also observed in both instances. In contrast, thermal dilation magnitudes and mechanisms vary from case to case, and are highly dependent on the materials and structural characteristics of specific bridges.

2. Study area and data stacks

Both the Rainbow Bridge and Lupu Bridge, carrying main traffic in and out of the Tianjin Zhongxin Eco-city and Shanghai Expo Park, were chosen as our study objects. Built between 1980s and early 2000s, the growing in-service time and greatly rising traffic loads increased the complexity of their maintenance. Geologically, both bridges are located on alluvial plains in the eastern coast of China where ground subsidence has always been one of the most severe and widespread geological hazards (Luo et al., 2014; Perissin et al., 2012; Shi et al., 2017). Therefore, bridges constructed on such a kind of soft soil are likely to be gradually destroyed, making periodical maintenance necessary (Cusson et al., 2011; Sousa and Bastos, 2013).

For the partially coherent arch bridges with complex structures, high-resolution X-band images are most suitable for investigating their deformation (Antonova et al., 2016; Qin et al., 2017a). Moreover, the successful launch and routine operation of Sentinel-1 satellite also provide easily and freely accessible C-band images with short perpendicular and temporal baselines (Rucci et al., 2012; Torres et al., 2012). Therefore, to evaluate the performance of SAR data of different bands for bridge SHM, both X-band images of 3×3 m resolution and C-band images of 5×20 m resolution were collected for this study.

2.1. Rainbow Bridge, Tianjin

Rainbow Bridge, built from 1996 to 1998, is a three-span reinforced concrete arch bridge, with a total length of 504 m (see Fig. 1a). Both the Pier 12 and Pier 15 are fixed bearings, while the Pier 13 and pier 14 are longitudinally movable. The main bridge, based on a rigid arch adapted to the load capacity of pier foundation, is balanced by horizontal flexible ties (Zhang, 2000). Connecting the Tanggu and Hangu districts of Tianjin, it is built on a marine-land interaction area filled with continental Tertiary and Quaternary sediments which have not been fully consolidated (Minissale et al., 2008). Therefore, the piers on the land are prone to subsidence due to the heavy traffic loads. In addition, the piers located in the water are subject to tidal erosion (Zhang, 2000).

In 2002, the Tianjin Municipal Engineering Design & Research Institute monitored the bridge and found cracks of different degrees on the main piers and expansion joints, as well as pits in pavement (see Fig. 1b). Due to the long-term overload operation, a 7×2 m² of collapse occurred in the Tanggu span in June 2010 (see Fig. 1b). In 2013, the pier 15 inclined toward the Tanggu District with the concrete cracking up to 0.6×0.8 m² in the bottom.

Three data stacks including 14 ascending Cosmo-SkyMed (Cosmo) Stripmap images acquired from 2013 to 2014 with the incidence angle of 31.127° , as well as 29 ascending and 53 descending Sentinel-1 images collected from 2015 to 2017, with the incidence angles of 33.684° and

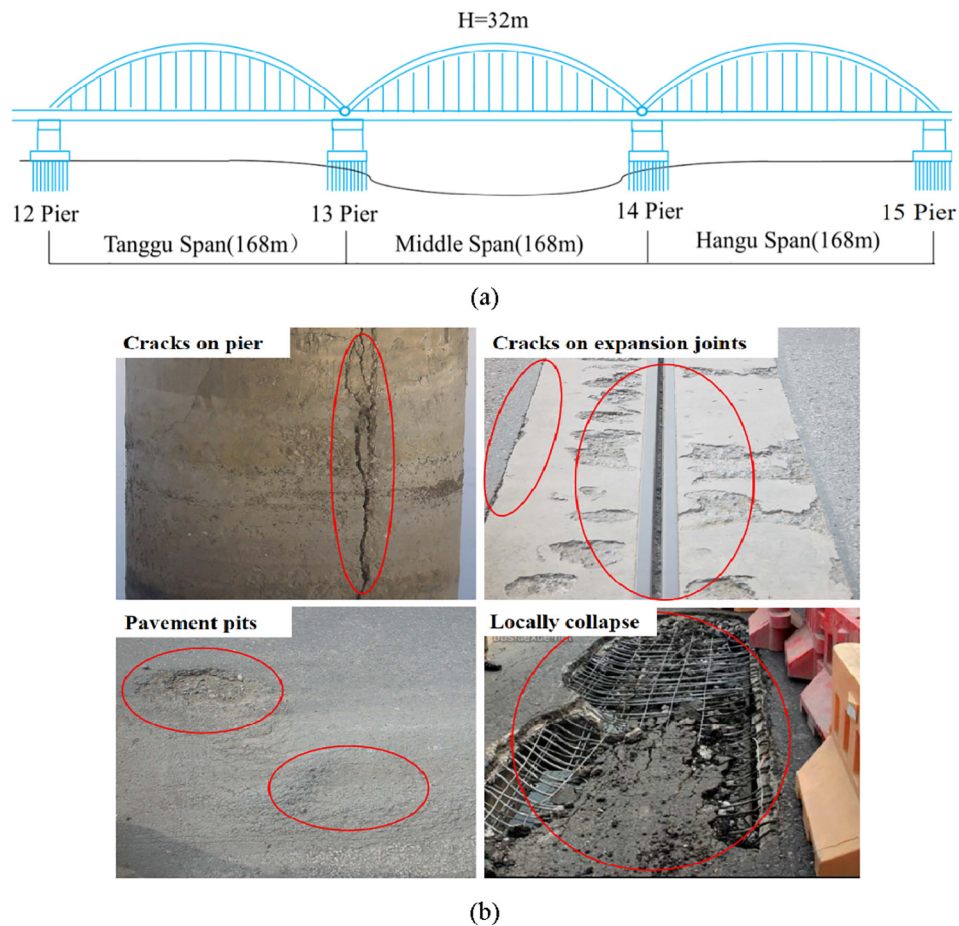


Fig. 1. Rainbow Bridge, (a) static scheme of the bridge; (b) in-situ photos of the damages.

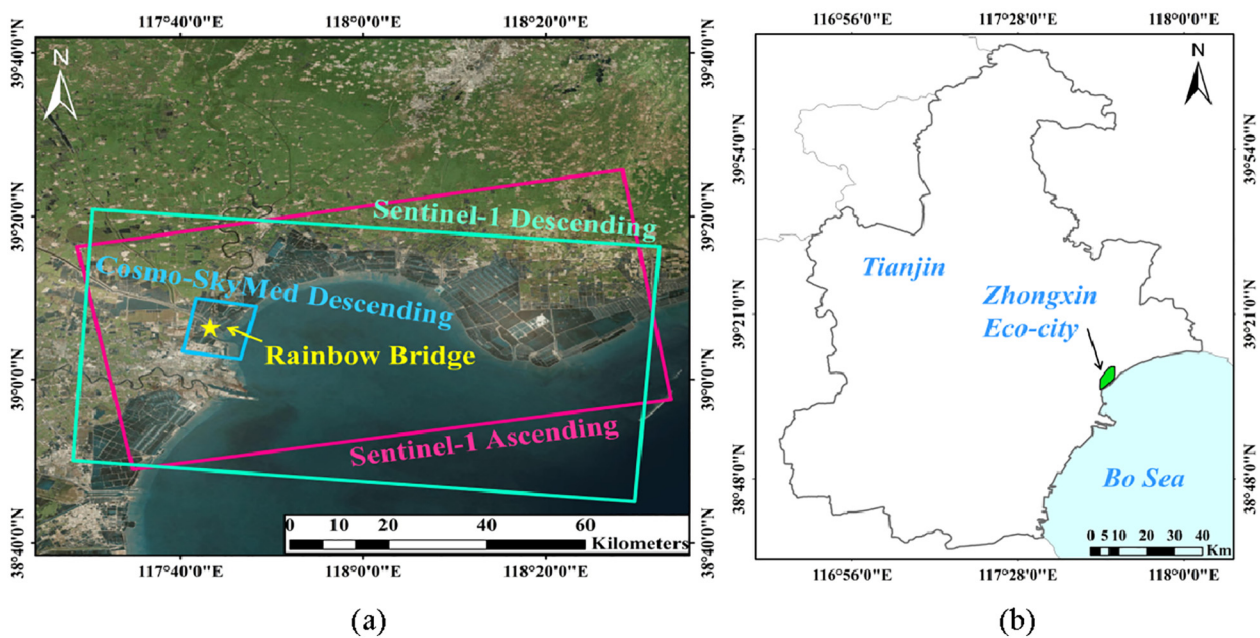


Fig. 2. (a) Google Map of Zhongxin Eco-city with the coverages of the three SAR data stacks and location of Rainbow Bridge; (b) location of Tianjin study area: the green polygon represents the Zhongxin Eco-city in (a). (For interpretation of the references to colour in this figure legend, the reader is referred to the web version of this article.)

34.034°, were analyzed to detect the deformation of Rainbow Bridge. Leveling measurements from 2013 to 2014 conducted at 128 points along the bridge deck were collected as reference data for DInSAR

result verification. The study area is illustrated in Fig. 2. The blue, red and green rectangles in Fig. 2a represent the coverages of the descending Cosmo, ascending and descending Sentinel-1 images,

Table 1Information for Cosmo data in Tianjin: acquisition date (Date), perpendicular (B_{perp}) and temporal (B_{temp}) baselines. Master image for PSI processing is 20130817.

No.	Date	B_{perp} (meters)	B_{temp} (days)	No.	Date	B_{perp} (meters)	B_{temp} (days)
1	20130310	622.9	-160	8	20130918	940.8	32
2	20130411	10.3	-128	9	20131020	-207.3	64
3	20130513	-94.6	-96	10	20131121	-329.1	96
4	20130614	604.5	-64	11	20131207	-233.1	112
5	20130716	-523.1	-32	12	20131223	71.4	128
6	20130817	0	0	13	20140124	675.4	160
7	20130902	-397.3	16	14	20140225	-876.1	192

Table 2

Information for ascending Sentinel-1 data in Tianjin. Master image for PSI processing is 20160508.

No.	Date	B_{perp} (meters)	B_{temp} (days)	No.	Date	B_{perp} (meters)	B_{temp} (days)
1	20150408	157.1	-396	16	20161104	23	180
2	20150502	-11.8	-372	17	20161116	71.2	192
3	20150526	-59.1	-348	18	20161128	98.6	204
4	20150701	-15.7	-312	19	20161210	53.6	216
5	20150725	-86.8	-288	20	20161222	21.8	228
6	20150818	16.7	-264	21	20170103	24.1	240
7	20150911	31.8	-240	22	20170115	50.2	252
8	20160109	110.2	-120	23	20170127	64.6	264
9	20160226	15.3	-72	24	20170208	76.1	276
10	20160508	0	0	25	20170220	34.9	288
11	20160601	29.6	24	26	20170304	55.2	300
12	20160719	66.8	72	27	20170316	7.4	312
13	20160929	54.4	144	28	20170328	66.7	324
14	20161011	-10.6	156	29	20170409	-19	336
15	20161023	-36.1	168				

Table 3

Information for descending Sentinel-1 data in Tianjin. Master image for PSI processing is 20160525.

No.	Date	B_{perp} (meters)	B_{temp} (days)	No.	Date	B_{perp} (meters)	B_{temp} (days)
1	20150401	-8.2	-420	28	20160407	76.6	-48
2	20150519	28.9	-372	29	20160419	46.7	-36
3	20150531	138.2	-360	30	20160513	-19.7	-12
4	20150612	94.2	-348	31	20160525	0	0
5	20150624	23	-336	32	20160606	51.5	12
6	20150706	-55	-324	33	20160630	59.4	36
7	20150718	52.6	-312	34	20160712	-53.5	48
8	20150730	94.9	-300	35	20160817	56.1	84
9	20150811	10.7	-288	36	20160829	28.2	96
10	20150823	55	-276	37	20160928	82.3	126
11	20150916	-40	-252	38	20161010	55.7	138
12	20150928	41	-240	39	20161022	-29.9	150
13	20151010	41.5	-228	40	20161103	93.4	162
14	20151022	-40.9	-216	41	20161115	60	174
15	20151103	32.7	-204	42	20161127	75.7	186
16	20151115	70.2	-192	43	20161209	51.2	198
17	20151127	110.5	-180	44	20161221	49.7	210
18	20151209	153.4	-168	45	20170102	75.8	222
19	20151221	40.5	-156	46	20170114	111.9	234
20	20160102	36.1	-144	47	20170126	85.8	246
21	20160114	-15.8	-132	48	20170207	52	258
22	20160126	-25.5	-120	49	20170219	18.9	270
23	20160207	123.2	-108	50	20170303	-77.4	282
24	20160219	72.7	-96	51	20170315	48.5	294
25	20160302	-18.1	-84	52	20170327	80.5	306
26	20160314	-49.3	-72	53	20170408	51.7	318
27	20160326	53	-60				

respectively. The yellow star indicates the location of the Rainbow Bridge. The green polygon in Fig. 2b denotes the Zhongxin Eco-city. Detailed information about the three SAR datasets is summarized in Tables 1–3. The perpendicular (B_{perp}) and temporal (B_{temp}) baselines of Sentinel-1 data are small. The X-band Cosmo data however, have large perpendicular baselines.

2.2. Lupu Bridge, Shanghai

Lupu Bridge, built from 2000 to 2003, is the second longest steel arch bridge in the world, with a single span of 550 m across the Huangpu River. The static scheme of the bridge is shown in Fig. 3a, in which A, C and D are longitudinal moveable bearings and only B is a fixed bearing. Using strong horizontal cables on both side-spans to balance the horizontal thrust of mid-span arch ribs, it is adapted for the

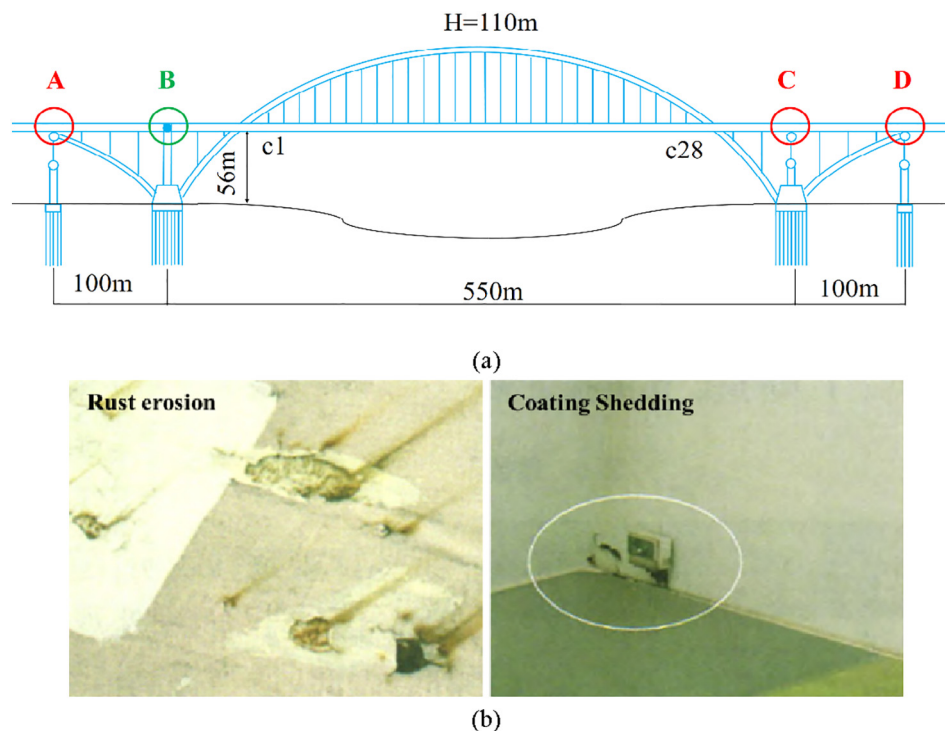


Fig. 3. Lupu Bridge, (a) static scheme of the bridge; (b) in-situ photos of the damages.

soft soil foundation in Shanghai (Ni, 2005). The main adverse engineering geological conditions that affect the stability of Lupu Bridge including the liquefied sand layer foundation, and the lack of dark green hard soil (Zhang et al., 2004).

Just before the opening of Shanghai Expo in 2010, the bridge management departments carried out a health examination of the Lupu Bridge and found some rust erosion as shown in Fig. 3b, which might indicate potential risks to the bridge. Therefore, they immediately repaired the steel arch of the bridge.

Due to the ranging nature of the radar, a single SAR dataset can only measure the one-dimensional (1D) line-of-sight (LOS) displacements. The generally low-incidence angles make the DInSAR measurements mostly sensitive to uplift or subsidence, which limits the accurate inversion of horizontal deformation especially for the north-south direction because it is approximately normal to the LOS direction (Qin et al., 2017b). The joint utilization of ascending and descending geometries allows us to increase the number of measurements on a bridge in different LOS directions and makes the 3D separation of deformation along the longitudinal, lateral, and vertical directions of bridges feasible (Hu et al., 2012; Yang et al., 2017). Therefore, a stack of descending TerraSAR-X (TSX) Stripmap images with the incidence angle of 26.423° , as well as two sets of ascending and descending Cosmo images with the incidence angles of 31.933° and 21.7° , acquired from 2009 to 2010, were analyzed to retrieve the 3D deformation of Lupu Bridge. Another descending TSX data stack collected from 2013 to 2016 was used to further verify the estimated thermal dilation model of the bridge. The study area is illustrated in Fig. 4. The red, green and yellow rectangles in Fig. 4a represent the coverages of two descending TSX, ascending and descending Cosmo data stacks, and the green star indicates the location of Lupu Bridge. The green polygon in Fig. 4b denotes the location of Expo Park in Shanghai. The basic information of these data stacks collected in Shanghai is given in Tables 4–7. All the datasets have small perpendicular and temporal baselines, yielding high quality results.

3. Methodology

A structure-driven multi-temporal DInSAR approach for arch bridge-specific SHM was developed in this study. As shown in Fig. 5, the overall technical framework started from the original data collection and aimed to improve the reliability of PTs identification, thermal dilation separation, and structural risk assessment by introducing three structure-driven steps.

In the data collection stage, both high-resolution X-band images and medium-resolution C-band datasets were collected to evaluate the performance of bridge SHM based on different bands of SAR images. Moreover, the structural information, temperature records, and leveling data of bridges were also integrated into data processing and result interpretation. The SAR data in this study were processed with StaMPS, and three structure-driven improvements have been implemented to overcome the three main problems (see in Fig. 5) that hindered the widespread application of DInSAR-based Bridge SHM.

3.1. Single-bounce PTs densification

The SAR data is difficult to interpret because its oblique scene illumination may cause ghost signals in SAR images, which poses a greater challenge of object interpretation than that in optical images (Soergel et al., 2008). Moreover, the arch bridges in SAR images are vulnerable to de-correlation problems related to the vibration caused by environmental factors and specular backscattering of flat bridge deck. Therefore, the identification of a large number of PTs on arch bridges is much more difficult compared to other types of man-made objects.

In order to distinguish useful signals from the ghost signals when identifying PTs on bridges, the backscattering characteristics of complex bridge structures must be considered (Soergel et al., 2008). The cross-water bridges in SAR images, usually exhibited as three parallel structures including the single-bounce, double-bounce, and triple-bounce signals, are illustrated in Fig. 6a, where h and b are the height and width of the bridge, and θ indicates the incidence angle of satellite (Qin et al., 2017a).

Taking the Lupu Bridge as an example, different types of

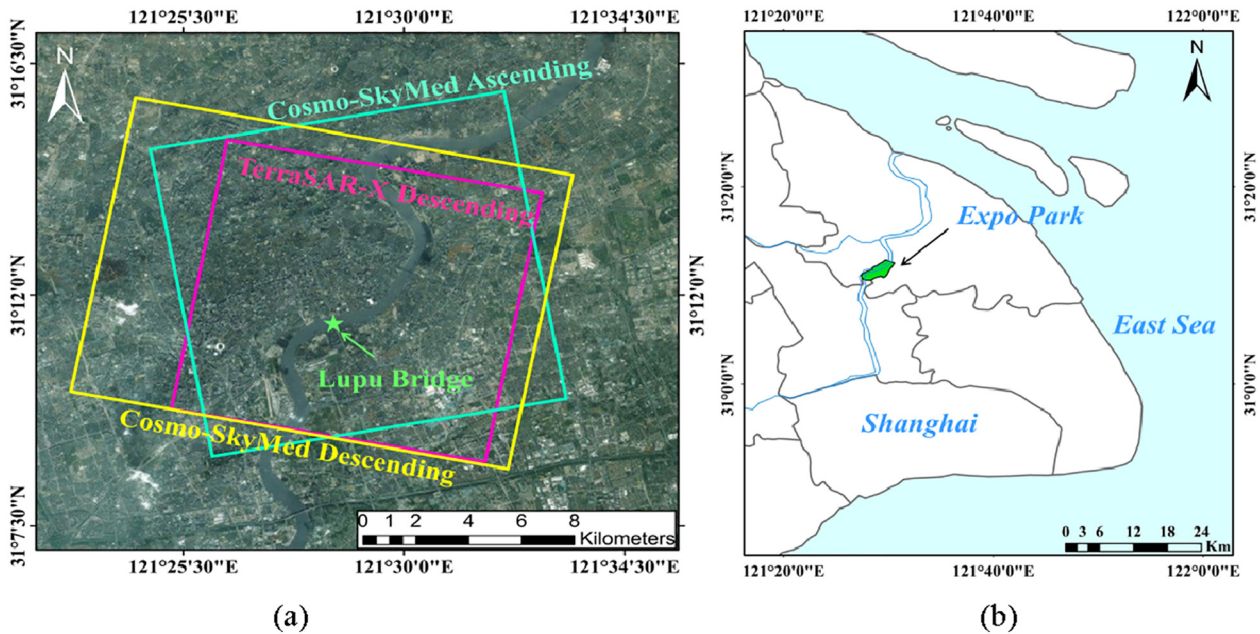


Fig. 4. (a) Google Map of Shanghai Expo Park with the coverages of the four SAR data stacks, and location of Lupu Bridge; (b) location of Shanghai study area: the green polygon represents the Shanghai Expo Park in (a). (For interpretation of the references to colour in this figure legend, the reader is referred to the web version of this article.)

backscattering lead to the appearance of three structures at different range locations in the TSX image (see Fig. 6b). Only single-bounce signals were observed on the arch, while three kinds of signals of the bridge deck appeared in SAR images. Usually, the single-bounce signals are mainly visible on the outline of structures, and probably reflected from metal railing elements. The double-bounce signals produced the brightest stripe due to the strong backscattering from structures similar to corner reflectors, and the triple-bounce stripe showed the weakest backscattering signal with the longest propagation path and power attenuation. According to the backscattering characteristics analysis, the deformation of main bridge is exactly associated with single-bounce signals, while both the double-bounce and triple-bounce stripes are virtual objects that should be excluded when estimating the bridge deformation.

The specific procedure for bridge single-bounce PTs identification applied in this study is shown in Fig. 7. Based on the backscattering geometrical interpretation, an approach that effectively combines the PTs selection strategies of PSI and SBAS interferometric processing, as well as the structural information of specific bridge, was implemented to improve the spatial density and accuracy of detectable single-bounce PTs upon bridges.

In the standard StaMPS PSI processing, an initial selection based on amplitude analyses is performed at first, and then the phase analysis is used to refine the PS probability by an iterative process (Ferretti et al.,

2001; Hooper et al., 2004; Hooper et al., 2007). In this study, different sets of PT candidates were selected by two individual indicators of amplitude and coherence, rather than being refined from the previous PT candidates. Therefore, the number of PT candidates by merging individual candidate sets of PTs is supposed to be larger than that of the standard StaMPS PSI processing, so as to detect more PT candidates on the bridges. Firstly, the statistical values of backscattering signals, including the mean amplitude and amplitude deviation, of the time-series SAR images were used as the incoherent observations to identify a set of PT candidates that maintain strong and stable backscattering over a long time. Then, the temporal coherence estimated from the time-series PSI interferograms was also used to select another set of dense PT candidates with small phase noise. By merging these two sets of PT candidates, the PTs identify abilities of both coherent and incoherent information in SAR images can be fully complemented to maximize the number of detectable dominant scatterers on bridges.

On the other hand, the spectrally-filtered interferograms with Small Baselines were also used to minimize the spatial/temporal de-correlation so that the semi-stable scatterers on bridge deck can be detected (Hooper, 2008). Since the PSI and SBAS methods select different but partially overlapping sets of points from different sets of interferograms, the multi-temporal method can combine them to extract signals from much more PTs with higher signal-to-noise ratio (SNR) than either method can achieve alone, permitting robust deformation

Table 4
Information for ascending Cosmo data in Shanghai. Master image for PSI processing is 20090815.

No.	Date	B_{perp} (meters)	B_{temp} (days)	No.	Date	B_{perp} (meters)	B_{temp} (days)
1	20090111	371.1	-216	11	20091002	607.5	48
2	20090212	113.9	-184	12	20091010	172.4	56
3	20090228	-370.3	-168	13	20091018	-77.2	64
4	20090316	-212.9	-152	14	20091026	-223.7	72
5	20090401	593.4	-136	15	20091103	-229.9	80
6	20090409	474.4	-128	16	20091205	499.4	112
7	20090604	-295.3	-72	17	20091213	322.4	120
8	20090612	579.7	-64	18	20091221	80.3	128
9	20090714	-386.9	-32	19	20100207	352.6	176
10	20090815	0	0				

Table 5

Information for descending Cosmo data in Shanghai. Master image for PSI processing is 20090825.

No.	Date	B_{perp} (meters)	B_{temp} (days)	No.	Date	B_{perp} (meters)	B_{temp} (days)
1	20090105	-740.4	-232	11	20090926	-700.4	32
2	20090113	-170	-224	12	20091004	-361.7	40
3	20090310	301.7	-168	13	20091020	457.7	56
4	20090326	-122	-152	14	20091028	553	64
5	20090411	-492.4	-136	15	20091105	624.6	72
6	20090521	703.3	-96	16	20091207	60.3	104
7	20090708	255.4	-48	17	20091223	459	120
8	20090716	203.1	-40	18	20091231	281.8	128
9	20090825	0	0	19	20100201	50.4	160
10	20090910	-101.7	16				

estimation. For each overlapped point, a weighted mean value for the phase was calculated by summing the phases from both datasets. The SNR of each dataset was estimated as the weight (Hooper, 2008; Hooper et al., 2007; Qu et al., 2015):

$$\text{SNR} = \frac{1}{\gamma_m^{-1} - 1} \quad (1)$$

$$\gamma_m = \frac{1}{N} \left| \sum_{i=1}^N \exp\{j(\varnothing_{m,i} - \tilde{\varnothing}_{m,i} - \Delta\varnothing_{\theta,m,i})\} \right| \quad (2)$$

In above equation, γ_m is used to evaluate the phase stability for the m th point, $\varnothing_{m,i}$ indicates the interferometric phase, $\tilde{\varnothing}_{m,i}$ represents the estimated spatially-correlated components of the phase, $\Delta\varnothing_{\theta,m,i}$ denotes the spatially-uncorrelated look angle error term, and N is the number of interferograms.

After the integration of above PT candidates, a posteriori pixel selection strategy was carried out to remove the unreliable points according to the local geolocation and elevation analysis of bridges (Qin et al., 2017b). Regarding the geolocation, PTs falling outside of a local buffer zone of the precise geo-located bridge single-bounce stripe in the longitude-latitude plane were excluded. In the elevation direction, PTs with elevation estimates that exceeded three times the standard deviation of the surrounding detected points were considered to be abnormal and filtered out because the elevations of points along a bridge are supposed to be successive. With this method, points located on other objects which are close to bridge structures can be successfully removed.

3.2. Thermal dilation separation and validation

In the case of bridges, especially for steel bridges like the Lupu Bridge, thermal dilation is often a key component of the interferometric phase signal, which would have a significant impact on DInSAR products if not properly handled during analysis (Fornaro et al., 2013; Lazecky et al., 2017; Huang et al., 2017). That is why a good knowledge of thermal dilation is essential to a quality Structural Health Monitoring of bridges, to avoid the thermal dilation mask small-amplitude deflection increases (Burdet, 2010).

Table 6

Information for descending TSX data from 2009 to 2010 in Shanghai. Master image for PSI processing is 20090920.

No.	Date	B_{perp} (meters)	B_{temp} (days)	No.	Date	B_{perp} (meters)	B_{temp} (days)
1	20090328	23.8	-176	10	20091012	-18.3	22
2	20090408	103.2	-165	11	20091023	-92.7	33
3	20090419	3.6	-154	12	20091114	44.8	55
4	20090511	23.7	-132	13	20091206	138	77
5	20090522	87.7	-121	14	20091217	148.5	88
6	20090602	91.4	-110	15	20091228	186.1	99
7	20090624	-64.1	-88	16	20100108	30.5	110
8	20090829	-158.7	-22	17	20100119	33.6	121
9	20090920	0	0	18	20100130	-68.5	132

Most previous studies modeled thermal dilation by adding a temperature dependent phase term into the traditional 2D (linear velocity and topographic error) analysis model, or by using a periodic seasonal phase term, which relied on model hypotheses (e.g. the linear deformation model) of PTs deformation (Monserrat et al., 2011; Fornaro et al., 2013; Crosetto et al., 2015). In the StaMPS analysis, no prior knowledge of deformation pattern is required, and the total deformation signals are separated from other phase components through the spatial-temporal filtering (Hooper et al., 2007). Then, based on an empirical model in which the thermal dilation phases are linearly related to the temperature variation, the thermal dilation of PTs is estimated from the time-series deformation using a least-squares regression analysis. The specific procedures of thermal dilation estimation and validation are described in the following.

After removing the topographic phase, the orbital and atmospheric components were separated by spatial-temporal filtering, and the total time-series displacements of each PTs were calculated. However, when we analysis these time-series displacements, the periodical thermal dilation and random noise still remained as residual components which obscure the desirable surface displacements. With the assumption that the random noise is quite small on a given PT with high SNR, the residual components were dominated by thermal dilation (Milillo et al., 2016). To better distinguish the periodical thermal dilation from the surface deformation, the time-series differential interferograms and unwrapped images were visually analyzed to qualitatively evaluate the distribution and variation of thermal dilation. Based on these analyses, the thermal dilation was then quantitatively detected by considering its relationship with acquisition temperatures and its possible principle on arch bridges.

According to our investigation, thermal dilation of arch bridges, depending on their structural characteristics, tends to propagate from the piers to the spans. The horizontal deformation caused by thermal dilation would be balanced by the strong horizontal cables on side-spans mentioned above. Therefore, the accumulated thermal dilation usually causes the gradual downward bending of bridge deck (see Fig. 8), leading to the change in the vertical displacements (ΔD) of span-points, or the vertical length (ΔL) variation of tensile structures such as suspenders. Moreover, the temperature variation (ΔT) is approximately

Table 7
Information for descending TSX data from 2013 to 2016 in Shanghai. Master image for PSI processing is 20141201.

No.	Date	B_{perp} (meters)	B_{temp} (days)	No.	Date	B_{perp} (meters)	B_{temp} (days)
1	20130416	-56.8	-594	20	20141201	0	0
2	20130508	-84.3	-572	21	20141223	-43.9	22
3	20130530	26.2	-550	22	20150310	255.8	99
4	20130621	-27.6	-528	23	20150401	-87.3	121
5	20130713	-221.4	-506	24	20150515	-93.2	165
6	20130804	-34.3	-484	25	20150617	-54.4	198
7	20130826	-74.1	-462	26	20150720	-112.4	231
8	20130917	-94.9	-440	27	20150822	-183.9	264
9	20131009	-358.7	-418	28	20150924	-171	297
10	20131122	-179.7	-374	29	20151027	-94	330
11	20131214	-186	-352	30	20151129	-106.4	363
12	20140312	-104.4	-264	31	20151221	17.4	385
13	20140517	-32.7	-198	32	20160329	-110.8	484
14	20140711	-35.3	-143	33	20160501	-33.8	517
15	20140802	-45.8	-121	34	20160603	121.2	550
16	20140824	22.9	-99	35	20160706	64.4	583
17	20140915	52.3	-77	36	20160808	-64	616
18	20141007	-219.8	-55	37	20160910	-42.9	649
19	20141029	-126.2	-33	38	20161013	-195.8	682

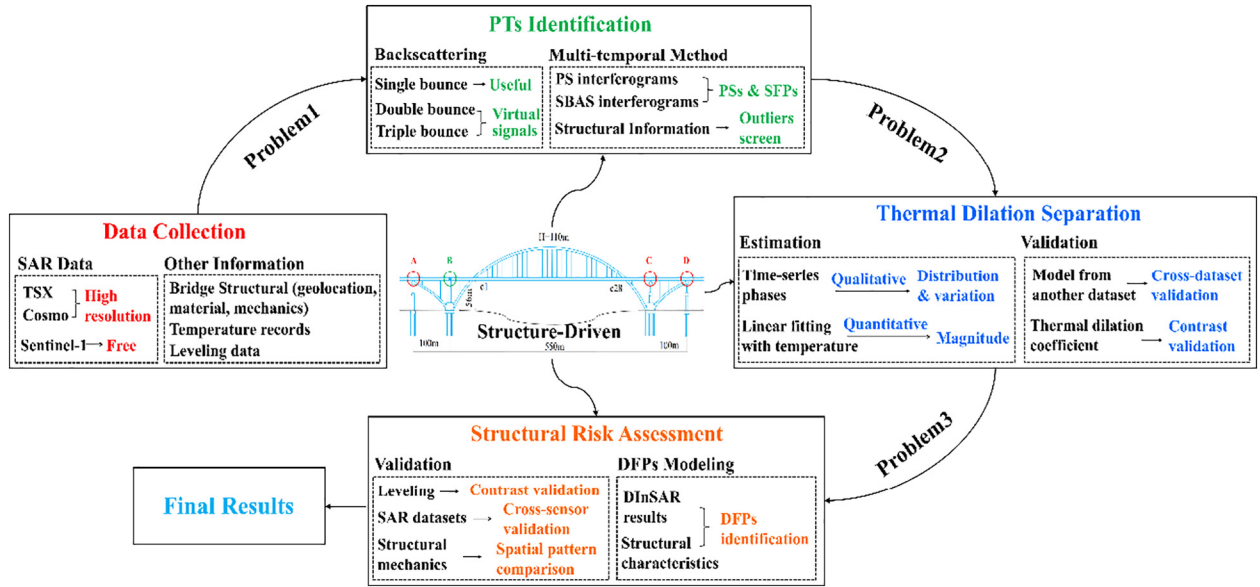


Fig. 5. Overall technical framework of structure-driven multi-temporal DInSAR approach.

proportional to ΔD or ΔL within a certain temperature range (Guo and Zhang, 2017). Therefore, we quantitatively modeled the thermal dilation by using a linear regression analysis between the ΔD or ΔL and the corresponding ΔT , which is given by:

$$\begin{cases} \Delta D = k \cdot \Delta T + b / \Delta L = k \cdot \Delta T + b \\ \Delta D = [\Delta D_1, \dots, \Delta D_N]^T / \Delta L = [\Delta L_1, \dots, \Delta L_N]^T \\ \Delta T = [\Delta T_1, \dots, \Delta T_N]^T \end{cases} \quad (3)$$

Assuming that the temperature is homogeneous along a bridge, the temperature deformation parameter k (mm/C) and constant b can be accurately estimated. For the suspenders, when ΔL equals to zero, ΔT will be $-b/k$. Considering the master temperature is T_m , the reference temperature (T_r) can be calculated by Eq. (4), which means that when the temperature is T_r , there is no thermal dilation on the structure, or else thermal dilations become observable. Moreover, the linear thermal dilation coefficient c ($/C$) of the material can be estimated by Eq. (5), which is supposed to be consistent with the actual physical property of the construction material.

$$T_r = -b/k + T_m \quad (4)$$

$$c = \Delta L / (L \cdot \Delta T) = (k + b) / (L \cdot \Delta T) \quad (5)$$

3.3. Structural risk assessment

Both the Rainbow and Lupu bridges are partially coherent structures in SAR images, meaning that some of their structural elements such as piers are coherent, while other parts like spans are incoherent. Therefore, the detection of deformation upon the whole bridge is complex and challenging. To solve this problem, we developed a DFPs model to effectively identify and classify the key points on bridge structures, so that the full scale structural risk assessment can be achieved by investigating the deformation at these limited DFPs.

The procedure for structural risk assessment on arch bridges applied in this article is shown in Fig. 9, among which the most important step is the DFPs identification. On one hand, the DFPs were identified in the coherent part of an arch bridge based on the spatial distribution and coherence of detected PTs upon the structure. On the other hand, PTs with large deformation velocities, or located at the structurally risky positions predicted from the structural mechanics analysis were also considered as the DFPs. Then, the DFPs identified on arch bridges were

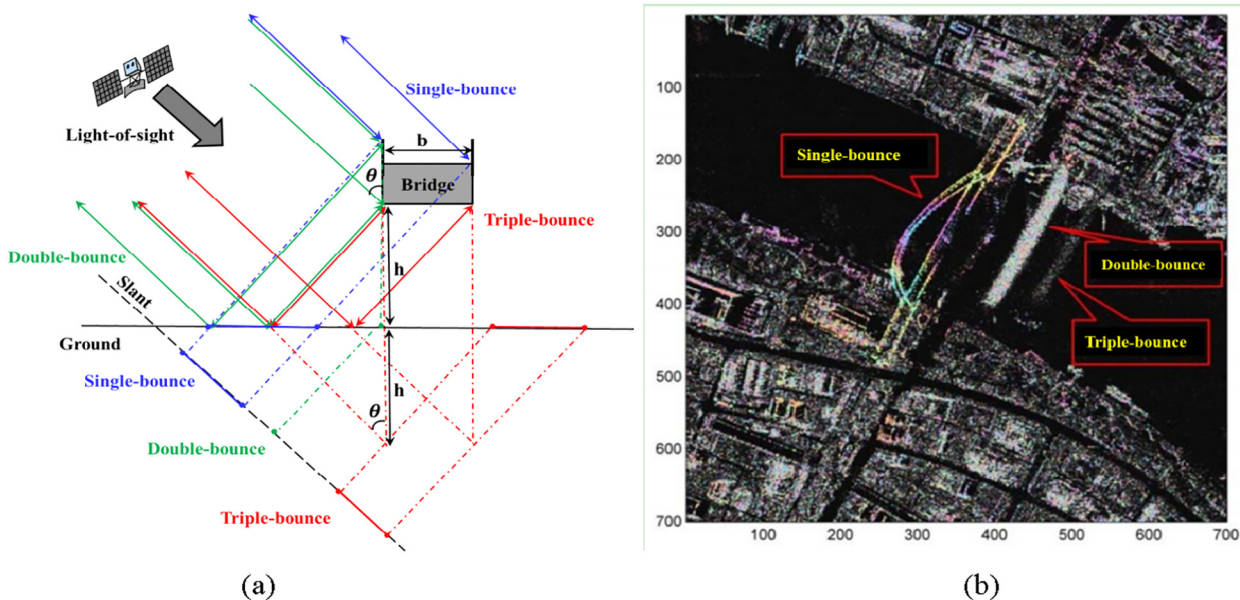


Fig. 6. (a) Multi-backscattering analysis of bridge; (b) Lupu Bridge in SAR image.

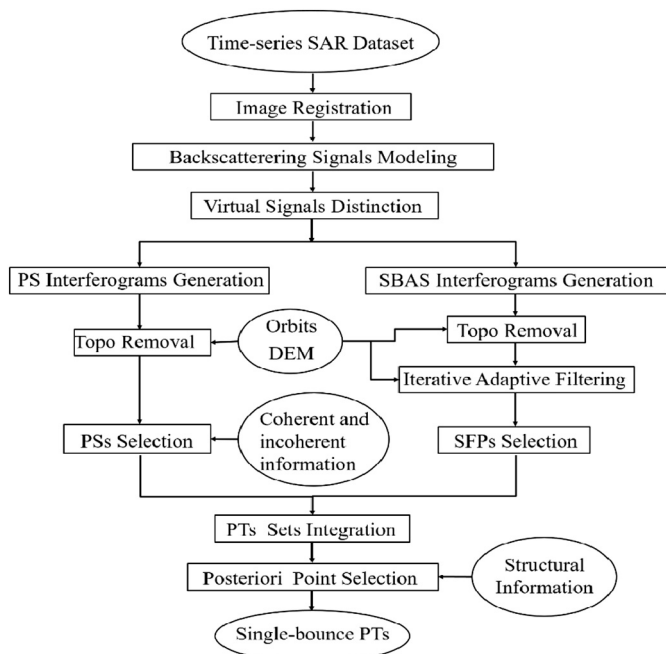


Fig. 7. Procedure of bridge single-bounce PTs identification.

classified according to their time-series displacements regularities. Since a bridge should be a continuous structure, the surface

deformation of sections without detectable PTs can be calculated by a proper interpolation, and the global deformation pattern along the bridges can be revealed. The reliability of our results were validated by comparing the deformation measurements against leveling benchmarks and cross-sensor results, as well as through the comparison between the estimated deformation patterns and the patterns predicted by structural mechanics principle. Finally, the structural risk level of the bridges was evaluated by qualitatively and quantitatively comparing the global deformation patterns retrieving from the DFPs measurements with the current technical specifications.

4. Results and validations

4.1. Rainbow Bridge

4.1.1. Results

Based on our approach, the LOS deformation velocity map of the Rainbow Bridge derived from Cosmo data (2013–2014) is shown in Fig. 10. Results of ascending and descending Sentinel-1 datasets (2015–2017) are illustrated in Fig. 11a–b. Displacement rates of –15 to 7 mm per year (mm/yr) were detected. The negative values indicate displacements moving away from the satellite, and the positive values imply movements approaching the satellite.

Apparently, the density of PTs identified from X-band SAR images (about 1200 PTs upon the bridge) is much larger than that of C-band images (about 500 PTs upon the bridge), and more deformation details can be found from X-band DInSAR results. Regarding the distribution regularity of PTs along the bridge, more PTs were identified around the

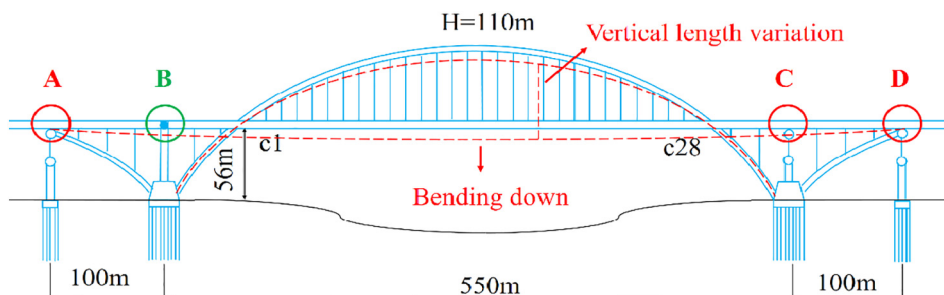


Fig. 8. Scheme for deformation caused by thermal dilation on arch bridges.

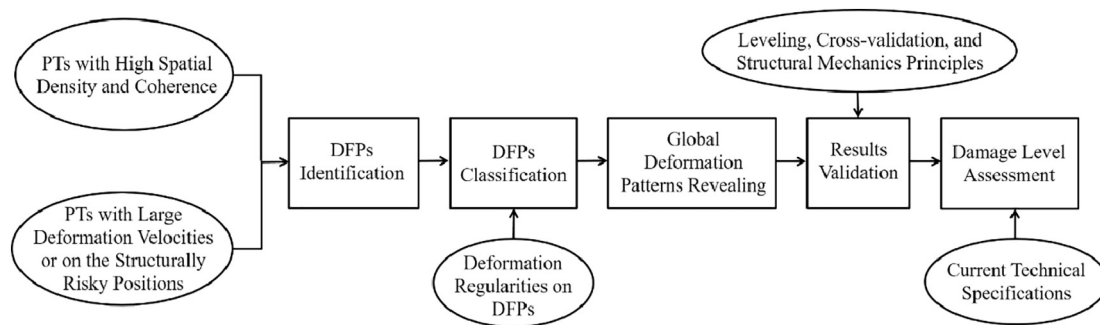


Fig. 9. Procedure for structural risk assessment on arch bridges.

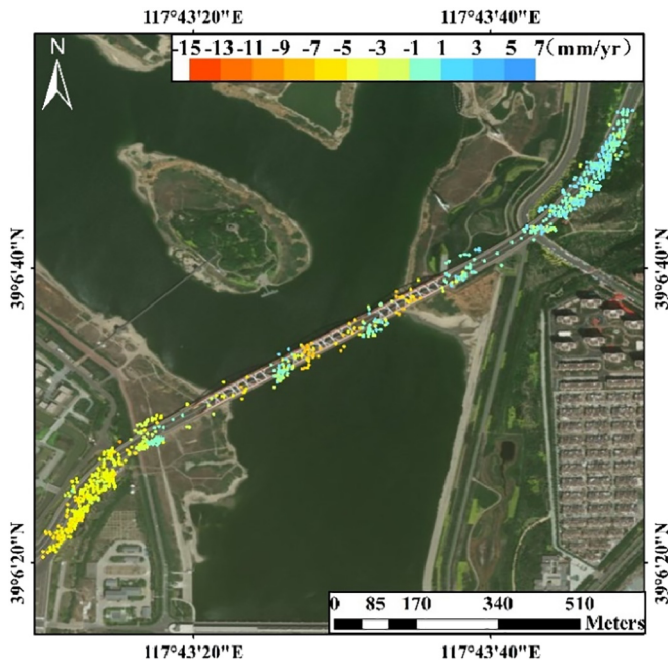


Fig. 10. LOS deformation velocities map of Rainbow Bridge from descending Cosmo data (2013–2014). Background image: Google Map.

piers and fewer were selected on the spans. All the results exhibit a similar deformation pattern, which is stable around the piers and subsidence on the central spans. Thus, both the PTs distribution and deformation patterns of the three distinct datasets are similar to each other.

However, due to the different observation periods, the deformation velocities of the Rainbow Bridge in Figs. 10 and 11 are slightly different and have decreased from the period 2013–2014 to the period 2015–2017. Moreover, the deformation of the sections on two river banks is most probably associated with the land subsidence. Since the Tangu District in the left is the old central district in Tianjin, its subsidence is larger than that of Hangu side in the right in the early stage (2013–2014). However, the subsidence of Hangu side increased recently due to the development of the Zhongxin Eco-city and surpassed that of the Tangu side, leading to a larger subsidence in the right bank between 2015 and 2017. The slight uplift on the other side may be caused by the groundwater recharge, or groundwater exploitation adjustment measures taken by the government (Luo et al., 2014).

4.1.2. Thermal dilation investigation

Based on the above results, the pier-points with high density and coherence, and span-points with large deformation, were identified as DFPs on the Rainbow Bridge. Their time-series displacements derived from Cosmo data (2013–2014) and the acquisition temperatures are

shown in Fig. 12a–b. The time-series displacements of PTs are different depending on their spatial locations on the bridge. As for pier-points, their displacements are almost linear and no evident thermal dilation effects were observed. The slight uplifts (< 1 mm) of the two middle piers could be caused by the upward thrusts which were generated to balance the long-term downward pressure of the two adjacent bridge spans. However, the displacements of span-points seemed to be temperature dependent, which were fast when the temperature is high and then slowly rebounded during the winter time. Since the number of Cosmo images in this study is limited and the observation period is less than one year, we just qualitatively argue that the thermal dilation of the Rainbow Bridge is mainly on the span and much less pronounced around the piers.

The two-year time-series displacements (2015–2017) of pier-points and span-points derived from ascending and descending Sentinel-1 data together with their acquisition temperatures are illustrated in Figs. 13 and 14. Comparing with Cosmo results, the deformation magnitudes of pier-points are slightly different due to the different observation periods. Since the time intervals of Cosmo images are much smaller and more uniform than those of Sentinel-1 images, the Cosmo time-series displacements of pier-points showed better continuity, while larger fluctuations were observed in the Sentinel-1 results.

The time-series analysis demonstrated that the thermal dilation effects on the displacements of span-points are significantly larger than those of pier-points. Similar time-series displacements of the three spans are observed, behaving obvious correlations with temperature variation due to the change in strength of pavement material. When the temperature is high, the stiffness of asphalt pavement decreases significantly, leading to the rapid subsidence under the surface traffic loads. During the winter time with lower temperature, the pavement is more stable with the enhanced hardness. Quantitatively, the maximum displacement gaps of the span-points are all about 15 mm between winter and summer, indicating a high consistency between the two independent results.

A least-squares regression analysis was carried out to investigate the thermal dilation effects on the displacements of span-points (see Fig. 15a–b), revealing strong linear correlations between the vertical subsidence difference (ΔD) and the temperature disparity (ΔT), with the R^2 of 0.8452 and 0.8894. Both the fitted models (remarked by the red lines) agreed well with each other, indicating a high reliability of our results.

4.1.3. Validation

In order to validate the reliability of DInSAR results, 128 leveling points measured once a year by the Trimble DINI Electronic Leveller from 2013 to 2014, which are evenly distributed on the upstream and downstream sides of the Rainbow Bridge (see Fig. 16), were used for comparison. According to the standard for Chinese secondary leveling measurements, the height accuracy of leveling was set to 2 mm/km.

A comparison of subsidence profiles along the bridge deck obtained by leveling and InSAR is shown in Fig. 17. In the upper half of this

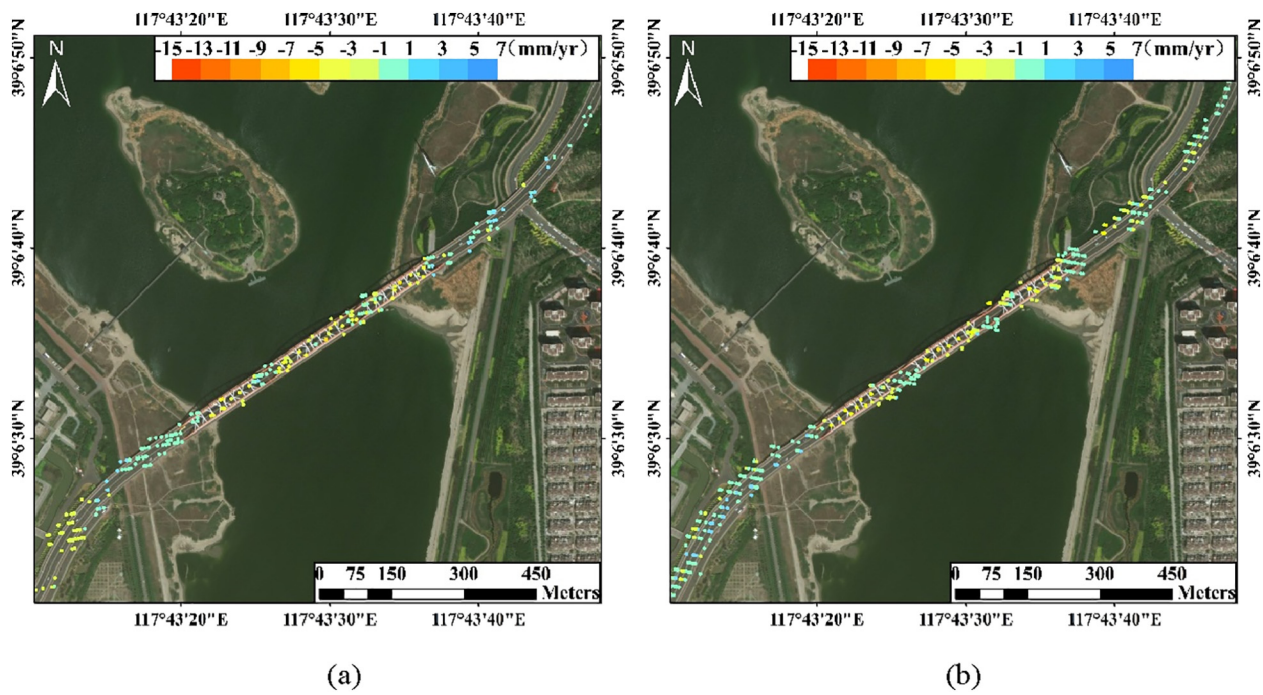


Fig. 11. LOS deformation velocities maps of Rainbow Bridge from (a) ascending and (b) descending Sentinel-1 data (2015–2017). Background image: Google Map.

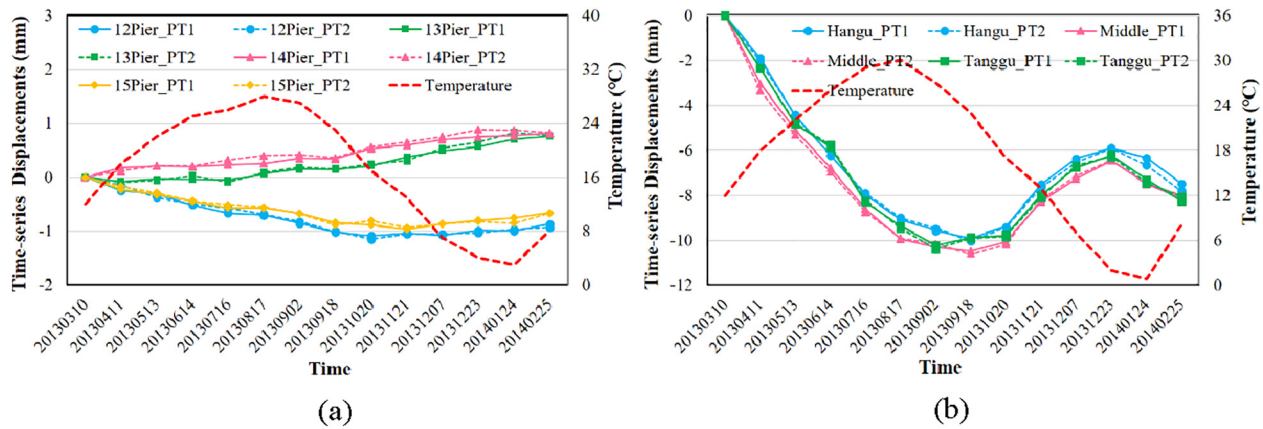


Fig. 12. Time-series displacements of (a) pier-points and (b) span-points on the Rainbow Bridge derived from Cosmo data.

figure, the green and orange lines denote the subsidence profiles measured by the upstream and downstream side leveling points respectively. Among leveling points, the subsidence is highly uncertain

because of the low point density. Fortunately, this low spatial density can be supplemented by the denser measurements derived from InSAR which are represented by the blue line in the lower half of Fig. 17.

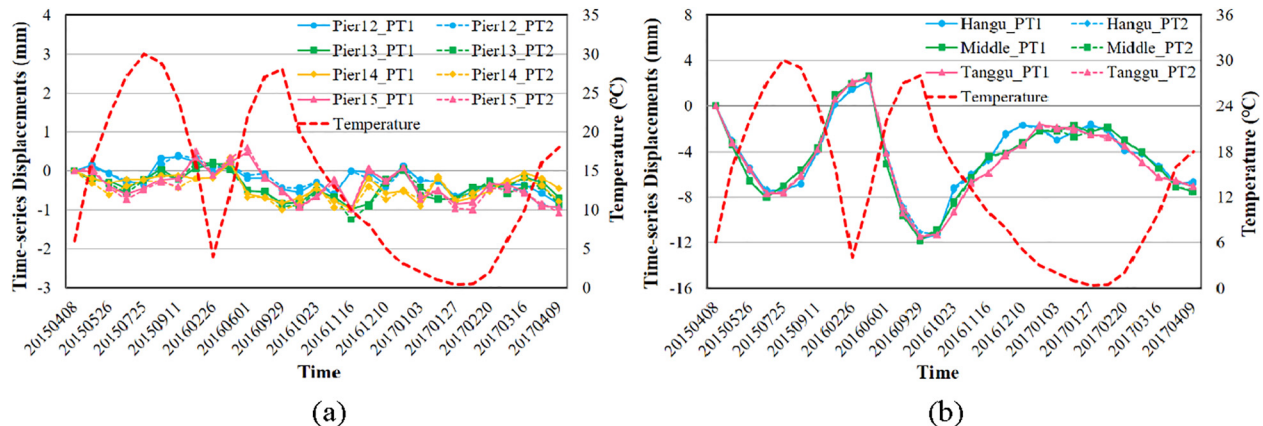


Fig. 13. Time-series displacements of (a) pier-points and (b) span-points on the Rainbow Bridge derived from ascending Sentinel-1 data.

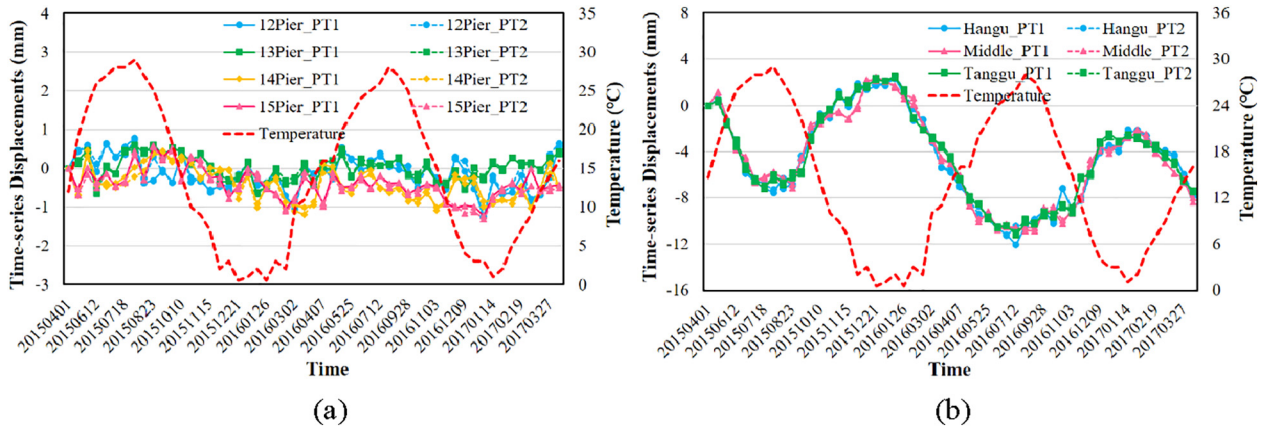


Fig. 14. Time-series displacements of (a) pier-points and (b) span-points on the Rainbow Bridge derived from descending Sentinel-1 data.

All the three profiles showed almost the same surface deformation pattern, which is stable around piers and subsidence on the spans. From the perspective of structural-reliability, the piers of the bridge, with deep pile foundations, always prevent deformation on the bridge deck. Therefore, the deformation around the four piers (remarked by the red boxes in Fig. 17) are small, which is consistent with the theoretical situation deduced from the structural mechanics principle, indicating the rationality of our results. However, a subsidence deviation of about 4 mm was observed at the evenly distributed leveling points around each pier, indicating that the subsidence around the piers was uneven distributed. Therefore, oscillations (less than ± 3 mm), also observed in the InSAR measurements around each pier, are reasonable because the pier-points are unevenly distributed on the bridge deck. Moreover, settlements on the three spans observed by leveling points are slightly smaller than those measured by InSAR, but still within a reasonable range. That may be because the leveling points were distributed at the positions of suspenders (see Fig. 16) where an upward tension might prevent the surface deformation, while the PTs on the bridge surface are farther away from the constraints of suspenders.

The average subsidence comparison on the four piers is shown in Fig. 18, where the blue triangles denotes the results of leveling, and the orange diamonds represents the average measurements from InSAR PTs which were within 5 m of the leveling points. The average subsidence differences from pier 12 to pier 15 are 0.97 mm, 1.62 mm, 1.51 mm, and 0.91 mm respectively, with an average value of 1.27 mm and a standard deviation of 2.95 mm, showing highly consistent between these two independent results.

The cross-validation of vertical subsidence velocity profiles derived from ascending (the blue solid line) and descending (the red dotted line) Sentinel-1 data (2015–2017) along the Rainbow Bridge is shown

in Fig. 19. The profile shapes agreed well with each other no matter in subsidence pattern and magnitude, and are also similar to the surface deformation pattern of Cosmo results (2013–2014).

4.2. Lupu Bridge

4.2.1. Results

Processing three different X-band SAR data stacks of the same period (2009–2010) independently, the LOS deformation velocity maps of the Lupu Bridge derived from the descending TSX, descending and ascending Cosmo datasets are shown in Fig. 20a–c. The PTs are concentrated on the piers and dispersed on the span, with the estimated subsidence rates ranging from -13 to 9 mm/yr. Results from the three data stacks showed a similar pattern of symmetrical progressive surface deformation, with the deformation areas occurred on the span and the stable segments appeared around the piers. However, the different incidence angles and acquisition dates inevitably led to slight differences in the LOS deformation velocities.

4.2.2. Thermal dilation modelling

Compared with C-band SAR images of the Rainbow Bridge, the high-resolution X-band data stacks of the Lupu Bridge displayed a higher level of sensitivity to thermal dilation and showed more detailed structural information of the arch and beam. Therefore, we further quantitatively investigated the thermal dilation of this steel bridge. By visually analyzed the time-series differential interferograms and unwrapped images in Fig. 21a–b, together with the temperature differences, we found that the Lupu Bridge suffered from a strong thermal dilation especially at the central span because the accumulation of thermal dilation signals in the middle of bridge span is evident. The

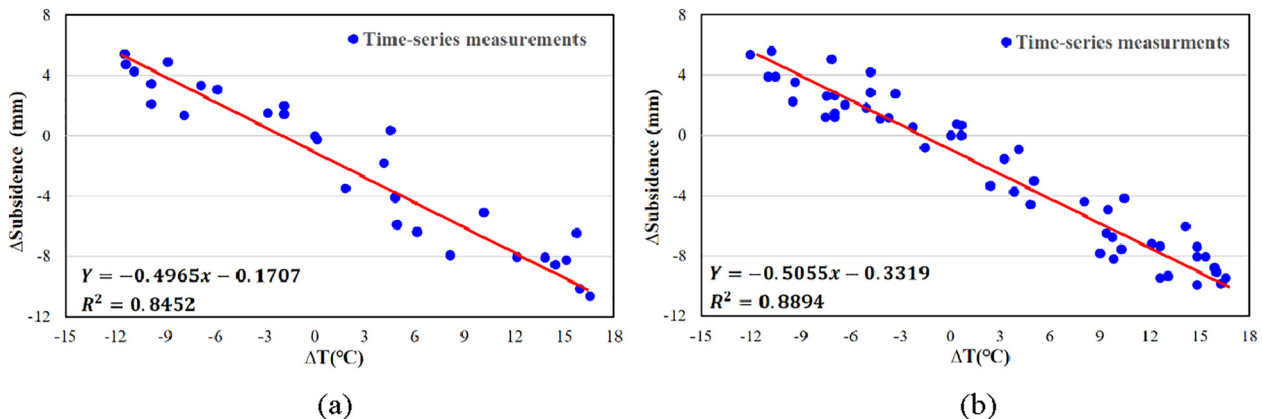


Fig. 15. Thermal dilation fitting of span-points on the Rainbow Bridge derived from (a) ascending and (b) descending Sentinel-1 results.

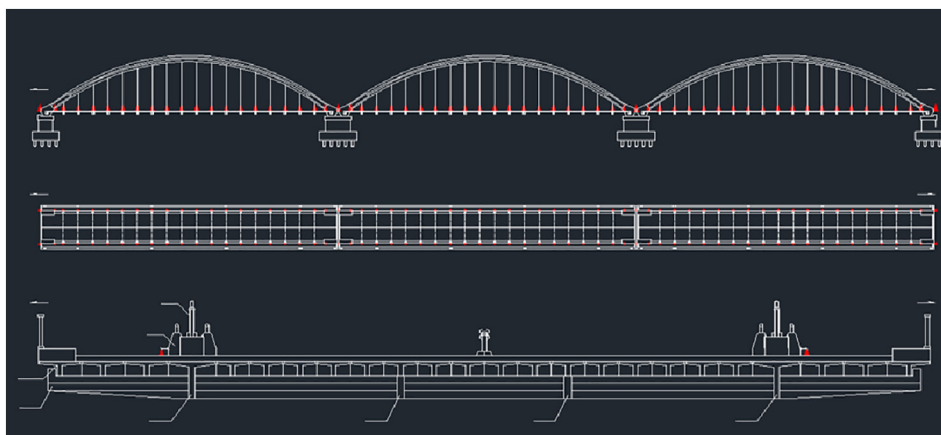


Fig. 16. Distribution of leveling points (the red points) on the Rainbow Bridge. (For interpretation of the references to colour in this figure legend, the reader is referred to the web version of this article.)

thermal dilation signals are visible in the differential interferograms with large temperature differences (remarked by the red rectangles), and disappeared in the other differential interferograms with small temperature disparities.

Based on the qualitative analyses of thermal dilation signals, we shifted focus to the quantitative detection of thermal dilation effects on span-points where the largest thermal dilation were observed. The time-series displacements of PTs on the middle of the dome and span (see green circles in Fig. 22) are represented by the green and blue lines respectively. Their slowly rebounding time-series displacements indicate that these are not permanent deformation. The red bold line is the temperature of the acquisition time. When the temperature goes up, the subsidence in the central span correspondingly increase, and vice versa, indicating a negative correlation between time-series displacements of span-points and temperature variation.

The suspenders, as the main load bearing components of an arch bridge, are composed of high-strength steel wire bunches, which are sensitive to the ambient temperature variation (Li et al., 2012). We calculated the vertical subsidence difference between the middle of the

dome and span (ΔL), and found a linear correlation with ΔT as shown in Fig. 23 (Guo and Zhang, 2017). The blue points indicate the time-series DInSAR measurements, and the red line is the linear fitting result between ΔL and ΔT . These two variables show quite a good linear relationship with the R^2 of fitted model being 0.8499. According to this model, when ΔL equals to zero, ΔT is about 12.84 °C. Since the T_m is 4.6 °C, the 17.44 (12.84 + 4.6) °C is approximately the reference temperature (T_r) for the bridge. Based on this T_r , the 1 °C change in temperature would lead to a vertical subsidence difference of about 9.86×10^{-6} of the suspenders' length. Actually, this estimated linear thermal dilation coefficient ($9.86 \times 10^{-6}/^\circ\text{C}$) is in accordance with the physical property of typical steel material which is usually in the range of $9\text{--}12 \times 10^{-6}/^\circ\text{C}$ (Ni et al., 2007), indicating high accuracy of the estimated thermal dilation.

Another time-series TSX dataset (2013–2016) was used to further verify the estimated thermal dilation model of the Lupu Bridge. The time-series displacements of the middle dome and span points are represented by the green and blue lines in Fig. 24. Similar as Fig. 23, a strong linear correlation between the calculated ΔL and ΔT (see Fig. 25)

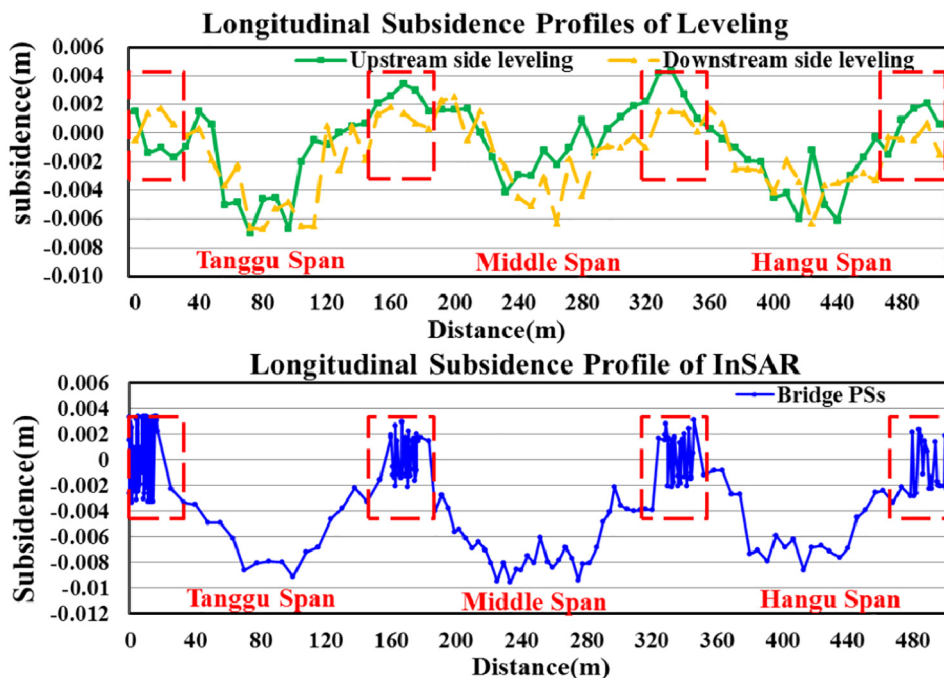


Fig. 17. Subsidence profiles of the Rainbow Bridge derived from Leveling (upper) and InSAR (lower).

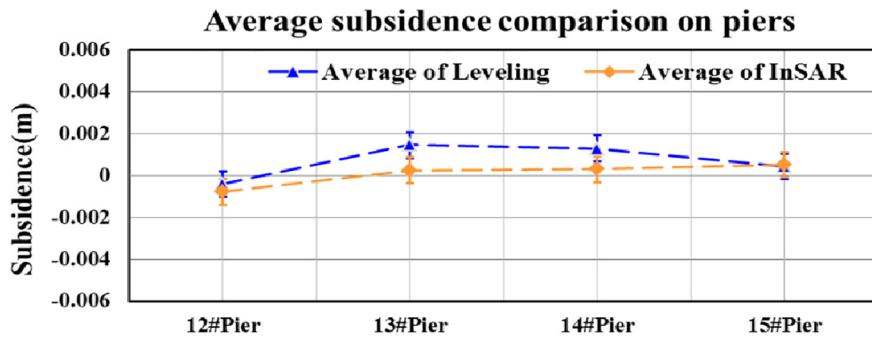


Fig. 18. Comparison of the average subsidence on four piers derived from Leveling and InSAR.

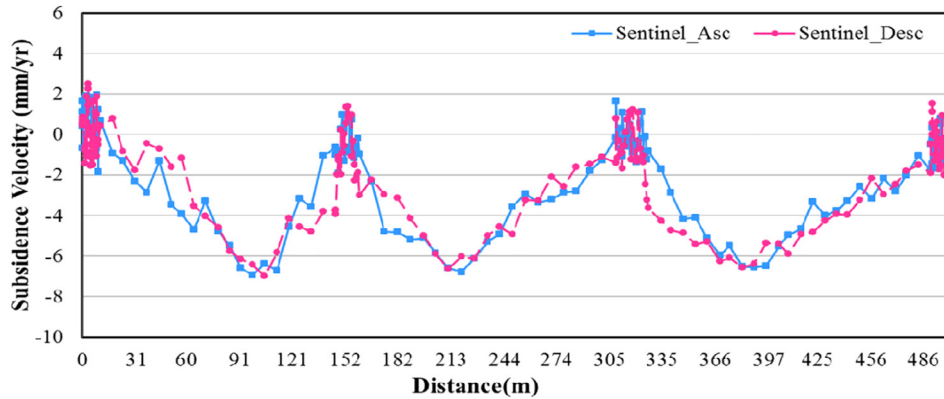


Fig. 19. Subsidence velocity profiles of the Rainbow Bridge from ascending (blue solid line) and descending (red dotted line) Sentinel-1 datasets. (For interpretation of the references to colour in this figure legend, the reader is referred to the web version of this article.)

was also found, with the R^2 as high as 0.9111. This linear model indicates that when ΔL equals to zero, ΔT is about -7.3°C . Since the T_m is around 25.3°C , the T_r is approximately $18 (-7.3 + 25.3)^\circ\text{C}$, which is close to 17.44°C calculated by datasets from 2009 to 2010. When the temperature change by 1°C , ΔL is about 10.08×10^{-6} of the suspenders' length, which is also within the reasonable range of linear thermal dilation coefficient of construction material.

Comparing these two thermal dilation models, we transferred them into the same basic temperature of 0°C as described in Eqs. (6) and (7),

and obtained two linear models (see Fig. 26). The green dotted line represents the linear model retrieved from 2009 to 2010 (Model1) and the red solid line indicates the linear model derived from 2013 to 2016 (Model2). It is clear that the difference of temperature deformation parameters (0.493 and 0.504) is within $0.02\text{ mm}^\circ\text{C}$. Moreover, the disparity of modeled ΔL is less than 1 mm, which revealed a high consistent between the two models and verified the reliability of our results.

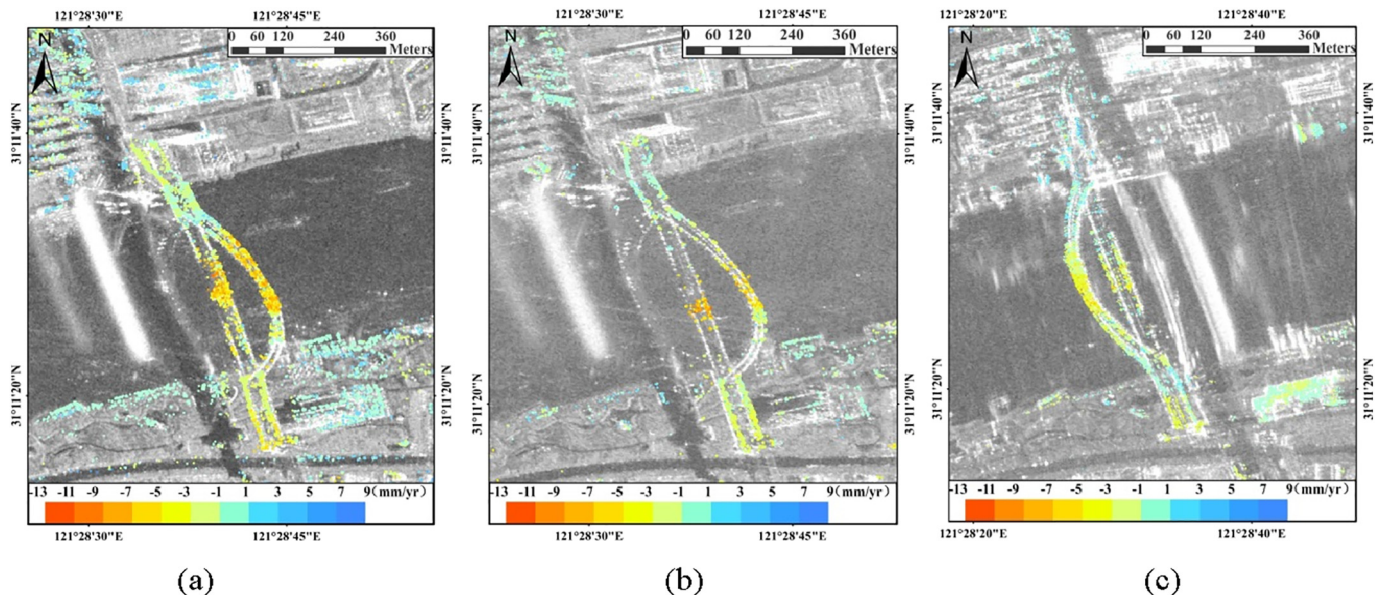


Fig. 20. LOS deformation velocities of the Lupu Bridge (2009–2010), (a) descending TSX data; (b) descending Cosmo data; (c) ascending Cosmo data.

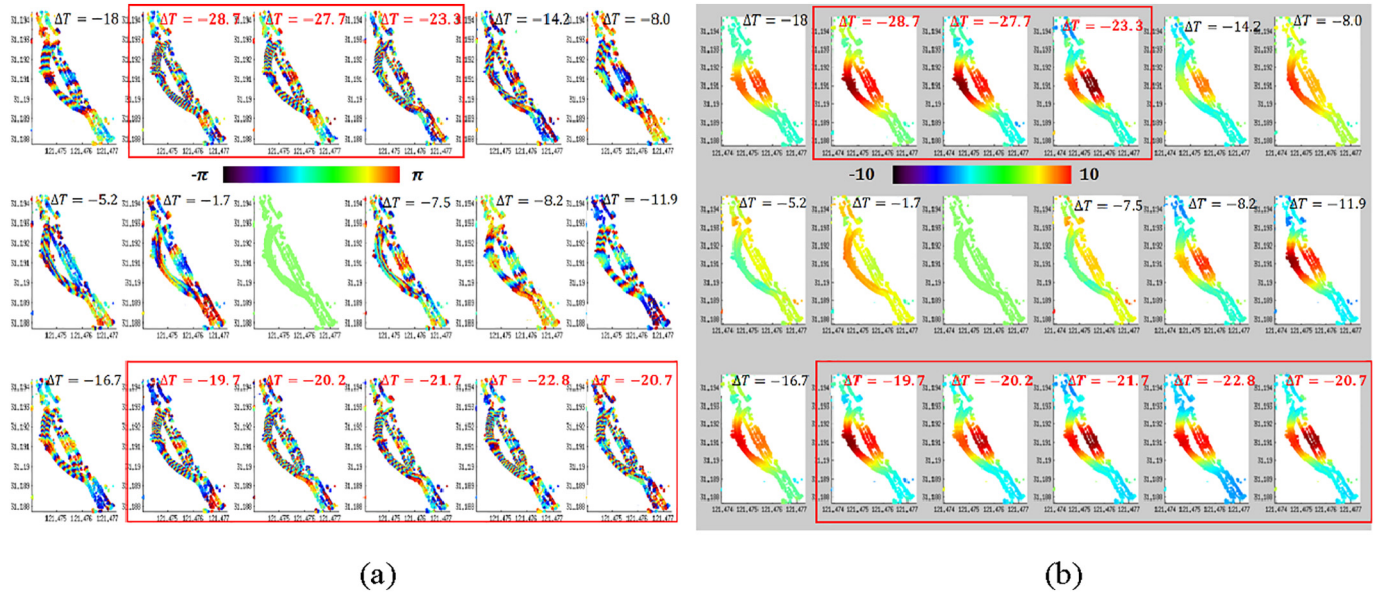


Fig. 21. Time-series (a) differential interferograms, and (b) unwrapped images, of the Lupu Bridge derived from ascending Cosmo data.

$$\text{Model1: } \begin{cases} Y = 0.493x - 6.332 \text{ (Based on } 4.6^\circ\text{C)} \\ Y = 0.493(x' - 4.6) - 6.332 = 0.493x' - 8.6 \text{ (Based on } 0^\circ\text{C)} \end{cases} \quad (6)$$

$$\text{Model2: } \begin{cases} Y = 0.504x + 3.624 \text{ (Based on } 25.3^\circ\text{C)} \\ Y = 0.504(x' - 25.3) + 3.624 = 0.504x' - 9.1 \text{ (Based on } 0^\circ\text{C)} \end{cases} \quad (7)$$

After further modeled and separated thermal dilation parameters of each PT on the bridge based on Model2, the final surface deformation and thermal dilation maps from 2013 to 2016 were produced (see Fig. 27). According to the surface deformation map on the upper half of this figure, the subsidence mainly occurred on the span, but much smaller (within 5 mm/yr), implying that the thermal dilation caused the majority of the observed deformation signals. The thermal dilation map on the lower half of the figure indicates that the thermal dilation is sensitive especially at the central span because a gradual accumulation of the temperature deformation parameters from the pier to the span was observed. The key physical property of material (the linear thermal dilation coefficient) and the static structural features (such as the

positions of piers) of the bridge can be inferred from the thermal dilation map through the magnitude and distribution pattern of thermal dilation parameters (Monserrat et al., 2011).

4.2.3. Validation

After removing the thermal dilation effects from 2009 to 2010 based on Model1, the cross-validation of vertical subsidence velocity profiles along the Lupu Bridge derived from three data stacks is shown in Fig. 28. The blue triangles and green dotted line indicate the results of ascending and descending Cosmo data, and the red solid line is derived from the descending TSX images. The red bold curve is the fitted deformation profile along the bridge. The results agreed well with each other on matter in the subsidence pattern or magnitude. All the three profiles showed a similar pattern of symmetrical progressive surface deformation, with the subsidence gradually increasing from the piers to the span, and peaking at the central span. This surface deformation pattern agrees well with the results derived by Zhao et al. (2017), and is also consistent with the structural mechanics principle as analyzed above. Quantitatively, all the maximum vertical subsidence velocities in the middle are about 8 mm/yr, showing strong consistency.

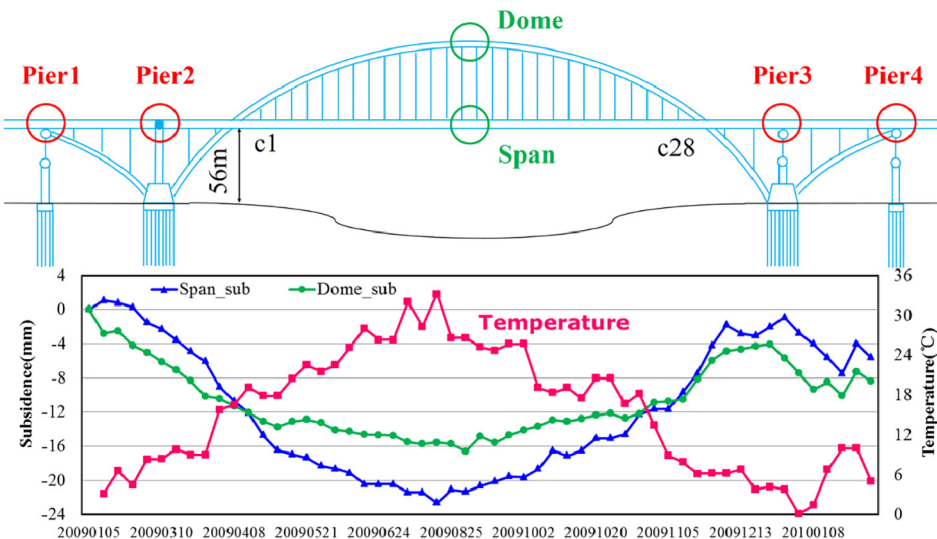


Fig. 22. Time-series displacements of the central Dome and Span points on Lupu Bridge (2009–2010).

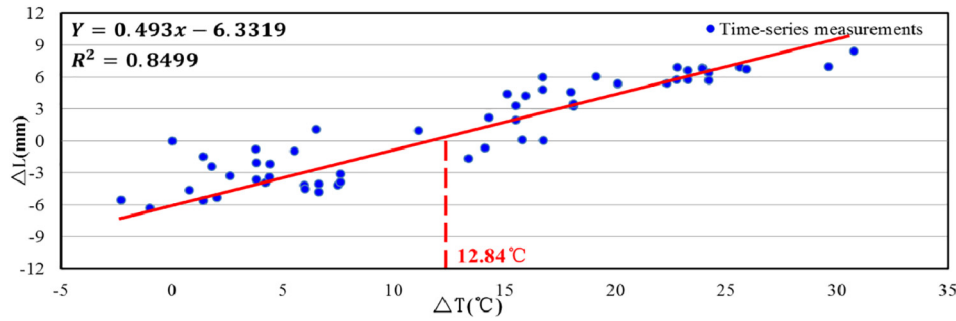


Fig. 23. Linear fitting results between ΔL and ΔT (2009–2010).

Given the three data stacks with the observation geometries illustrated in Fig. 29, the displacements of the bridge in the longitudinal, lateral and vertical directions were estimated and shown in Fig. 30. The red dotted line represents the vertical displacements, the blue solid line and green triangles indicate the deformation along the longitudinal and lateral directions respectively. Clearly, the deformation is dominant in the vertical direction, and the deformation of the middle span plays a major role because the side-spans are constrained strongly in vertical direction by piers. In contrast, the longitudinal displacements are much smaller due to the balance of strong horizontal cables mentioned previously. The lateral displacements are random with no specific deformation trend. Since lateral force would not be generated from the internal stress or traffic loads on such a straight bridge, they are most likely caused by the random crosswinds or possible measurement noise (Xu et al., 2010). The vertical deflection y in Fig. 30 along the bridge deck, which is a significant indicator describing the extent of structural damage, can be measured. Moreover, the deflection angle $\hat{\theta}$ in Fig. 30 can also be calculated by Eq. (8), where x indicates the distance from the fixed bearing to the point and y denotes the vertical deflection of the point.

$$\hat{\theta} \approx \tan \hat{\theta} = \frac{y}{x} \tag{8}$$

5. Discussion

Summarizing the results of the Rainbow and Lupu bridges, in both instances, similar characteristics including the PTs distribution, surface deformation pattern, and DFPs types were retrieved and effectively analyzed. Moreover, the difference in the thermal dilation, depending

on material and structural characteristics, were also observed. Finally, the structural risk levels reached on both bridges were evaluated based on the current technical specifications.

5.1. Similar characteristics for arch bridges

Three similar characteristics for arch bridges, such as the Rainbow and Lupu bridges, derived from this study are described in Table 8.

PTs detected on arch bridges, no matter on single-span or multi-span, are not evenly distributed along the structures. Their distribution is highly dependent on the static structural features of bridges, with more PTs concentrated around the piers and fewer PTs identified on the spans. This can be explained by structural theory. Since the bridges are hyper-static structures with redundant constraints on piers, the segments near piers are more stable than others, making it easier to detect dense PTs around the piers. The segments on the spans without any constraints however, are easily affected by the temperature, traffic loads, and wind on the structure, leading to dynamic changes in time-series SAR images. Thus, fewer PTs can be identified on the spans.

The surface deformation patterns of arch bridges exhibit a similar symmetrical progressive shape on a single span, with the largest displacements located at the central span and decreased toward the two ends. Therefore, for an arch bridge, the deformation occurs mainly on the spans while the segments near the piers are more stable. Such a surface deformation pattern is highly consistent with the structural mechanics principle of bridges because the piers with deep pile foundations usually act as the exterior constraints on the bridge structure, preventing the bridges from moving. Therefore, comparing the measured surface deformation pattern with the pattern inferred from the

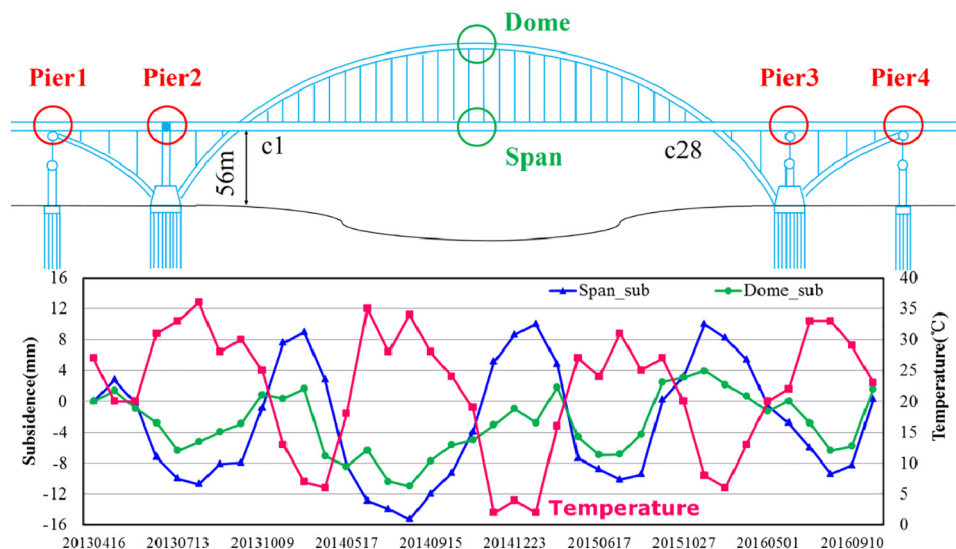


Fig. 24. Time-series displacements of the Dome and Span points on Lupu Bridge (2013–2016).

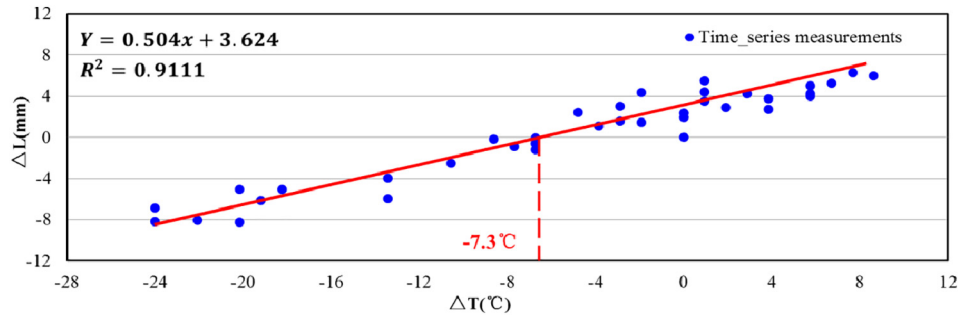


Fig. 25. Linear fitting results between ΔL and ΔT (2013–2016).

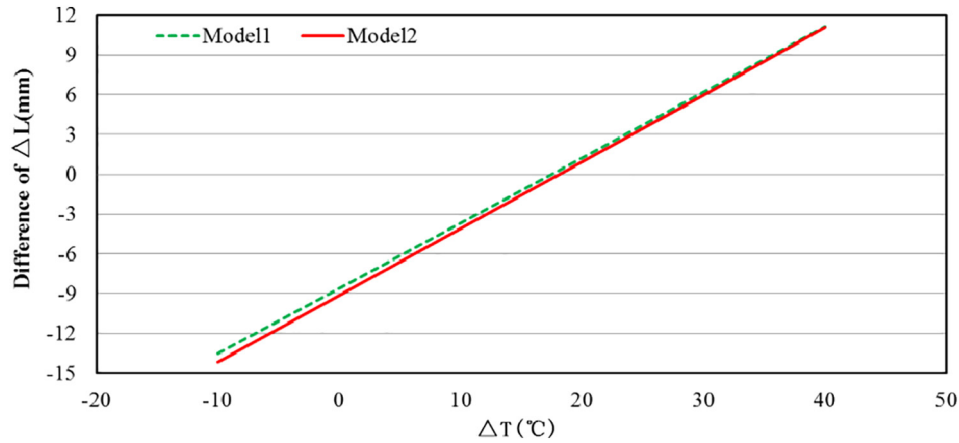


Fig. 26. Thermal dilation models of Lupu Bridge from 2009 to 2010 (Model1) and from 2013 to 2016 (Model2).

bridge mechanics principle, our results are reasonable.

In both cases, two kinds of DFPs on the partially coherent structures were identified. According to the structural characteristics and distribution of PTs, the pier-points, where the largest pressure act on and most PTs were identified, are significant in structural risk assessment. Meanwhile, based on the analysis of surface deformation pattern, the span-points, where the largest displacements usually occurred, are also

extremely worthy of attention when analyzing the structural health of bridges. By analyzing the surface deformation and thermal dilation on these two types of DFPs, the global deformation pattern can be revealed so as to achieve the structural risk assessment of partially coherent arch bridges in full scale.

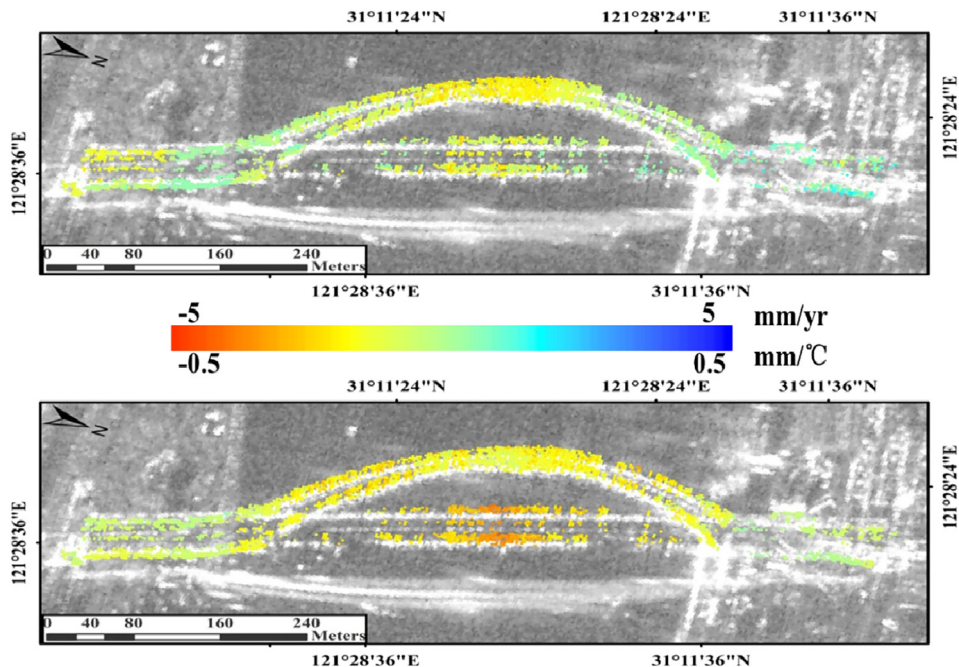


Fig. 27. Surface deformation map (upper) and thermal dilation map (lower) of the Lupu Bridge.

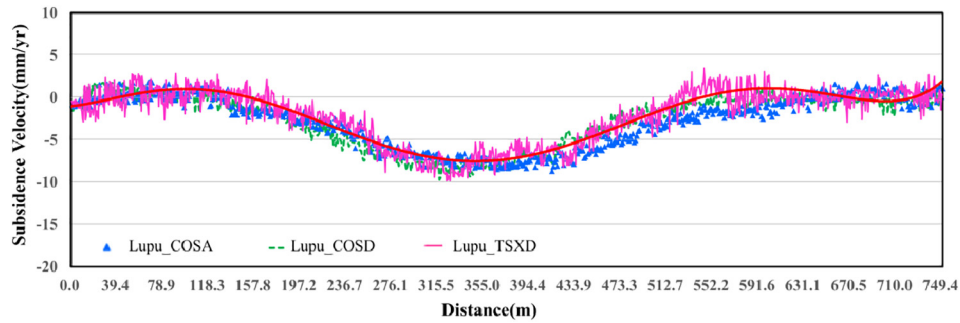


Fig. 28. Subsidence velocity profiles along the Lupu Bridge derived from ascending (blue triangles) and descending (green dotted line) Cosmo data, and descending TSX data (red solid line). (For interpretation of the references to colour in this figure legend, the reader is referred to the web version of this article.)

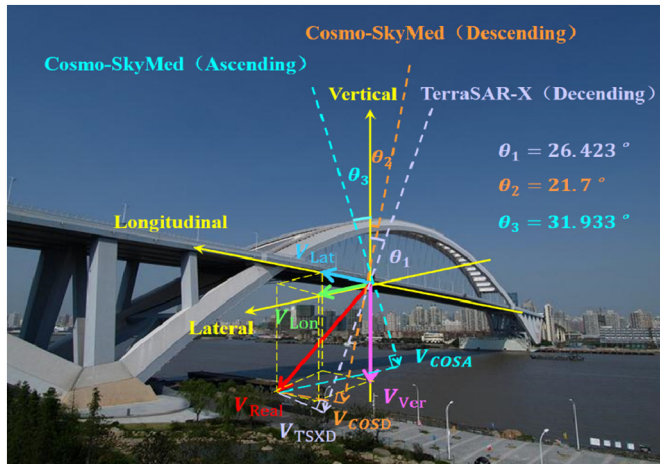


Fig. 29. Observation geometries of three SAR data stacks of the Lupu Bridge.

Table 8

Deformation characteristics for arch bridges.

Types	Qualitative Description
PTs Distribution	Not even; More around the piers; Less on the spans
Surface Deformation Pattern	Symmetrical progressive: starting from the piers and reaching a peak around the central spans
DFPs	Two types: pier-points; span-points

steel material used in Lupu Bridge (Ni et al., 2007; Yarnold, 2013). Therefore, the thermal dilation signals were less evident on the Rainbow Bridge. In terms of structural characteristics, the transmission of thermal dilation was interrupted by the presence of more piers on the Rainbow Bridge, limiting the effective transmission distance in a single span of 168 m and reducing the magnitude of thermal dilation. The thermal dilation on Lupu Bridge transmitted along a single-span of 550 m can increase to a much higher value without the interruptions from piers. Although the thermal dilation on each single span behaved similarly (evident in the central spans) on both bridges, different number and position of piers may lead to difference global thermal dilation patterns.

The thermal dilation mechanisms that observed on the two bridges are different. For the Rainbow Bridge, the periodical components of the displacements on central spans are most probably caused by the change in stiffness of the pavement material due to the temperature variation. Negative correlation between the vertical subsidence of span-points and temperature variation was observed from the fitted model. In the case

5.2. Different thermal dilation effects

The thermal dilation magnitude on the Rainbow Bridge is smaller than that of the Lupu Bridge, given the different material and structural characteristics. The material used in the Rainbow Bridge is the pre-stressed concrete, which, with a coefficient of thermal dilation lower than that of steel, is less sensitive to the temperature variation than the

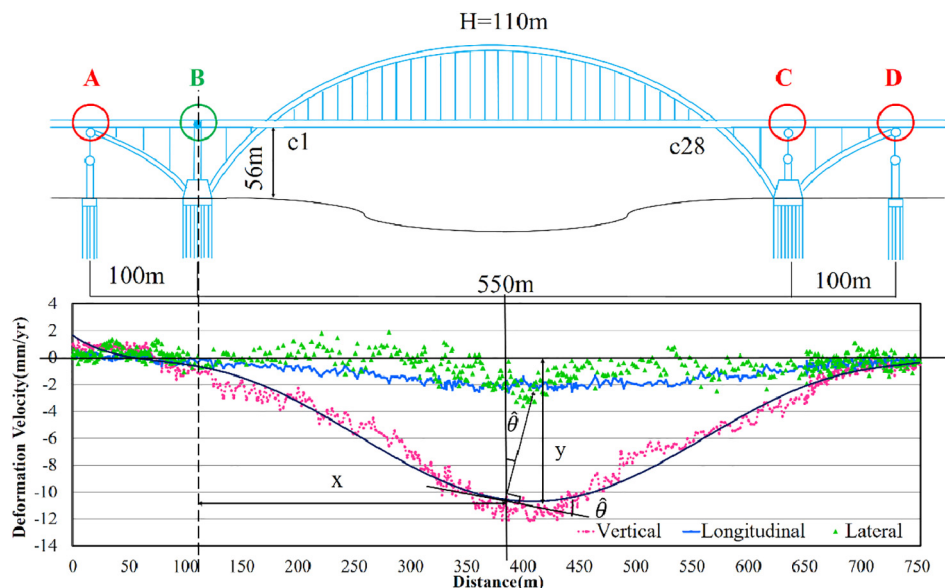


Fig. 30. 3D profiles along the Lupu Bridge derived from three SAR data stacks.

Table 9
The pre-designed deformation tolerances for arch bridges.

Damage level	Qualitative description	Quantitative description
1	Perfect or no obvious deformation on the beam	d_{max} close to 0
2	A certain amount of bending deformation on the beam; Slight vibration or shaking while driving and walking	$d_{max} < l/1000$
3	Deflection close to limit value; A serious permanent deformation on the beam	$l/1000 < d_{max} < l/600$
4	Deflection greater than limit value; A serious permanent deformation on the beam; Have significant impact on the bearing capacity and driving safety	$d_{max} > l/600$

of Lupu Bridge, more detailed information on the arch and beam were obtained from the X-band SAR images, and the time-series vertical ΔL of suspenders were measured. The temperature dependent displacements of the middle span are caused by the thermal expansion and contraction of the steel suspenders, and positive correlation between the vertical ΔL of suspenders and temperature variation was observed from the fitted model.

Overall, for different bridges, the thermal dilation should be analyzed depending on the specific material and structural characteristics, as well as their thermal dilation mechanisms.

5.3. Structural risk level assessment for arch bridges

To quantify the structural risk level of bridges, it is necessary to establish quantitative metrics for performance assessment based on the design specifications. The integration of related indicators from the “Technical Specification for Structural Safety Monitoring Systems of Highway Bridges (JT/T 1037-2016)” and “Technical Code for Test and Evaluation of City Bridges (CJJ/T 233-2015)” allowed us to determine the structural risk level reached on bridges. The pre-set deformation tolerances for arch bridges are illustrated in Table 9, where d_{max} indicates the largest middle-span deflection and l represents the length of the bridge. Calculating the deflection along the Rainbow and Lupu bridges according to their deformation profiles, the largest middle-span deflections are approximately $l/16000$ and $l/36000$ respectively (less than $l/1000$). Moreover, the largest displacements on the spans are elastic deformation rather than permanent deformation since slow rebounds were observed. Therefore, both the bridges are in the second security level according to Table 9, with a certain amount of bending deformation, and slight vibrations or shakes while driving and walking on them.

6. Concluding remarks

Arch bridges, as major transportation links in China, are vulnerable to considerable structural and functional deficiencies due to aging without routine inspection and maintenance. Therefore, the prompt and accurate deformation monitoring for them is of key importance in risk-hazard management for the responsible authorities. In this article, a structure-driven multi-temporal DInSAR approach was developed for arch bridge-specific SHM. In this method, the difficulties of selecting dense PTs on structures, separating the thermal dilation and surface deformation, and assessing global structural risk, in the traditional DInSAR-based bridge SHM, were addressed by introducing three structure-driven steps (i.e. backscattering geometrical interpretation, linear thermal dilation estimation and validation, and DFPs based risk assessment). The effectiveness of our approach is fairly presented by two case studies of the Rainbow and Lupu bridges using X-band and C-Band SAR data, and the experimental results were verified in different ways to show a millimeter-level precision. The proposed method can accurately assess structural risk on arch bridges by quantitatively characterizing their long-term surface deformation and thermal dilation. In summary, the following conclusions can be drawn:

The PTs detected on arch bridges are concentrated on the bridge piers thanks to the restrains from their deep pile foundations. Those on the bridge spans however, are sparse due to their variation and specular

backscattering of flat bridge deck in SAR images. Such pattern correlates strongly with the theoretical expected PTs distribution.

Thermal dilation of steel arch bridges (e.g. Lupu Bridge) are more obvious than those of concrete arch bridges (e.g. Rainbow Bridge), and their magnitudes and mechanisms depended highly on the material and structural characteristics of specific bridges. For verification, on one hand, the estimated thermal dilation coefficient of material used in the bridge was compared with the actual physical properties of material; on the other hand, comparative analysis between thermal dilation models derived from different SAR data stacks was carried out. Both of these results indicate the effectiveness of our method.

After separating the thermal dilation, the surface deformation patterns on arch bridges show a similar symmetrical progressive shape on a single span. In general, the segments near piers remain stable as opposed to the middle of spans that typically exhibit the maximum subsidence. This is also consistent with the deformation pattern inferred from their structural mechanics principle.

The qualitative and quantitative investigation of surface deformation regularities and thermal dilation for DFPs (mainly composed of pier-points and span-points) provide valuable information for the global deformation revealing and structural risk assessing on arch bridges. Both the Rainbow and Lupu bridges are in the second security level by comparing the qualitative and quantitative deformation measurements against the current technical specifications.

The potential of the structure-driven Multi-temporal DInSAR method for arch bridge SHM has been fully confirmed in our experiments. We also argue that it will be one of the key techniques to improve the next generation of smart bridges from their initial structural design to the later maintenance and management. More detailed study of investigating deformation characteristics for different types of bridges, and monitoring 3D bridge deformation by integrating multiple SAR sensors is needed in future research.

Acknowledgement

This work is supported by the National Natural Science Foundation of China [Grant No. 41571435,61331016], the Research Grants Council of Hong Kong Special Administrative Region [Grant No. PolyU 152043/14E, PolyU 152232/17E], and also the Innovation and Technology Fund [Grant No. GHP/006/14SZ]. [Grant No. 41571435, 61331016]. Thanks for the TSX images provided by DLR through the AO project [Grant No. MTH1743], Cosmo images from Vastitude Technology Co. Ltd., and leveling data of Remote Sensing Application Center of Ministry of House and Urban-Rural Development through the project [Grant No. 06-Y30B04-9002-13/15].

Conflicts of interest

None.

References

- Ahlborn, T.M., Shuchman, R., Sutter, L.L., Brooks, C.N., Harris, D.K., Burns, J.W., et al., 2010. Evaluation of commercially available remote sensors for highway bridge condition assessment. *J. Bridg. Eng.* 17 (6), 886–895. [http://dx.doi.org/10.1061/\(ASCE\)BE.1943-5592.0000303](http://dx.doi.org/10.1061/(ASCE)BE.1943-5592.0000303).
- Antonova, S., Käab, A., Heim, B., Langer, M., Boike, J., 2016. Spatio-temporal variability

- of X-band radar backscatter and coherence over the Lena river delta, Siberia. *Remote Sens. Environ.* 182, 169–191. <http://dx.doi.org/10.1016/j.rse.2016.05.003>.
- Berardino, P., Fornaro, G., Lanari, R., Sansosti, E., 2002. A new algorithm for surface deformation monitoring based on Small Baseline differential interferograms. *IEEE Trans. Geosci. Remote Sens.* 40 (11), 2375–2383. <http://dx.doi.org/10.1109/TGRS.2002.803792>.
- Beshr, E.W., 2015. Structural deformation monitoring and analysis of highway bridge using accurate geodetic techniques. *Engineering* 07 (8), 488–498. <http://dx.doi.org/10.4236/eng.2015.78045>.
- Beshr, E.W., Kaloop, M.R., 2013. Monitoring bridge deformation using auto-correlation adjustment technique for total station observations. *Positioning* 4 (1), 1–7. <http://dx.doi.org/10.4236/pos.2013.41001>.
- Burdet, O.L., 2010. Thermal effects in the long-term monitoring of bridges. In: International Association for Bridge and Structural Engineering Symposium, Venice, 2010 (76–68). <https://doi.org/10.2749/222137810796025465>.
- Casu, F., Manzo, M., Lanari, R., 2006. A quantitative assessment of the SBAS algorithm performance for surface deformation retrieval. *Remote Sens. Environ.* 102, 195–210. <http://dx.doi.org/10.1016/j.rse.2006.01.023>.
- Chang, L., Hanssen, R.F., 2014. Detection of cavity migration and sinkhole risk using radar interferometric time series. *Remote Sens. Environ.* 187, 49–61. <http://dx.doi.org/10.1016/j.rse.2014.03.002>.
- Chen, Z.W., Xu, Y.L., Xia, Y., Li, Q., Wong, K.Y., 2011. Fatigue analysis of long-span suspension bridges under multiple loading: case study. *Eng. Struct.* 33 (12), 3246–3256. <http://dx.doi.org/10.1016/j.engstruct.2011.08.027>.
- Crosetto, M., Monserrat, O., Cuevas-González, M., Devanthery, N., Luzi, G., Crippa, B., 2015. Measuring thermal expansion using x-band persistent scatterer interferometry. *ISPRS J. Photogramm. Remote Sens.* 100 (s1), 84–91. <http://dx.doi.org/10.1016/j.isprsjprs.2014.05.006>.
- Cusson, D., Lounis, Z., Daigle, L., 2011. Durability monitoring for improved service life predictions of concrete bridge decks in corrosive environments. *Comput. Aided Civ. Inf. Eng.* 26 (7), 524–541. <http://dx.doi.org/10.1111/j.1467-8667.2010.00710.x>.
- Ferretti, A., Prati, C., Rocca, F., 2001. Permanent scatterers in SAR interferometry. *IEEE Trans. Geosci. Remote Sens.* 39 (1), 8–20. <http://dx.doi.org/10.1109/36.898661>.
- Fornaro, G., Reale, D., Verde, S., 2013. Bridge thermal dilation monitoring with millimeter sensitivity via multidimensional SAR imaging. *IEEE Geosci. Remote Sens. Lett.* 10 (10), 677–681. <http://dx.doi.org/10.1109/LGRS.2012.2218214>.
- Guo, Y.L., Zhang, X.Q., 2017. Influences of temperature changes and cable length errors on tension structures using un-adjustable cable length design. *Chin. Civil Eng. J.* 50 (6), 11–22. <http://dx.doi.org/10.15951/j.tmgxcb.2017.06.002>.
- Hooper, A., 2008. A multi-temporal InSAR method incorporating both persistent scatterer and Small Baseline approaches. *Geophys. Res. Lett.* 35 (16), 96–106. <http://dx.doi.org/10.1029/2008GL034654>.
- Hooper, A., Zebker, H., Segall, B., Kampes, B., 2004. A new method for measuring deformation on volcanoes and other natural terrains using InSAR persistent scatterers. *Geophys. Res. Lett.* 31 (23), 1–5. <http://dx.doi.org/10.1029/2004GL021737>.
- Hooper, A., Segall, B., Zebker, H., 2007. Persistent scatterer interferometric synthetic aperture radar for crustal deformation analysis, with application to Volcán Alcedo, Galápagos. *J. Geophys. Res. Solid Earth* 112 (B7), B07407. <http://dx.doi.org/10.1029/2006JB00476>.
- Hu, J., Li, Z.W., Sun, Q., Zhu, J.J., Ding, X.L., 2012. Three-dimensional surface displacements from InSAR and GPS measurements with variance component estimation. *IEEE Geosci. Remote Sens. Lett.* 9 (4), 754–758. <http://dx.doi.org/10.1109/LGRS.2011.2181154>.
- Huang, Q.H., Michele, C., Oriol, M., Bruno, C., 2017. Displacement monitoring and modelling of a high-speed railway bridge using C-band Sentinel-1 data. *ISPRS J. Photogramm. Remote Sens.* 128, 204–211. <http://dx.doi.org/10.1016/j.isprsjprs.2017.03.016>.
- Invernizzi, S., Lacidogna, G., Manuella, A., Carpinteri, A., 2011. AE monitoring and numerical simulation of a two-span model masonry arch bridge subject to pier scour. *Strain* 47 (s2), 158–169. <http://dx.doi.org/10.1111/j.1475-1305.2010.00752.x>.
- Ismail, Z., Ibrahim, Z., Chao, A.O.Z., Rahman, A.G.A., 2012. Approach to reduce the limitations of model identification in damage detection using limited field data for nondestructive Structural Health Monitoring of a cable-stayed concrete bridge. *J. Bridge. Eng.* 17 (17), 867–875. [http://dx.doi.org/10.1061/\(ASCE\)BE.1943-5592.0000353](http://dx.doi.org/10.1061/(ASCE)BE.1943-5592.0000353).
- Ji, B.H., Fu, Z.Q., 2010. Analysis of Chinese bridge collapse accident cases in recent years. *Chin. Civil Eng. J.* 43 (S1), 495–498. <http://dx.doi.org/10.15951/j.tmgxcb.2010.s1.010>.
- Lan, H.X., Li, L.P., Liu, H.J., Yang, Z.H., 2012. Complex urban infrastructure deformation monitoring using high resolution PSI. *IEEE Sel. Top. Appl. Earth Observ. Remote Sens.* 5 (2), 643–651. <http://dx.doi.org/10.1109/JSTARS.2011.2181490>.
- Lazecky, M., Rapant, P., Perissin, D., Bakon, M., 2014. Deformation of highway over undermined Ostrava-Svinov area monitored by InSAR using limited set of SAR images. *Procedia Technol.* 16, 414–421. <http://dx.doi.org/10.1016/j.protcy.2014.10.107>.
- Lazecky, M., Hlavacova, I., Bakon, M., Sousa, J., Perissin, D., Patricio, G., 2017. Bridge displacements monitoring using space-borne X-band SAR interferometry. *IEEE J. Sel. Top. Appl. Earth Observ. Remote Sens.* 10 (1), 205–210. <http://dx.doi.org/10.1109/JSTARS.2016.2587778>.
- Li, D., Zhou, Z., Ou, J., 2012. Dynamic behavior monitoring and damage evaluation for arch bridges suspender using GFRP optical fiber bragg gratings sensors. *Opt. Laser Technol.* 44 (4), 1031–1038. <http://dx.doi.org/10.1016/j.optlastec.2011.10.014>.
- Luo, Q.L., Perissin, D., Lin, H., et al., 2014. Subsidence monitoring of Tianjin suburbs by TerraSAR-X Persistent Scatterers Interferometry. *IEEE J. Sel. Top. Appl. Earth Observ. Remote Sens.* 7 (5), 1642–1650. <http://dx.doi.org/10.1109/JSTARS.2013.2271501>.
- Milillo, P., Perissin, D., Salzer, J.T., Lundgren, P., Lacava, G., Milillo, G., Serio, C., 2016. Monitoring dam structural health from space: insights from novel InSAR techniques and multi-parametric modeling applied to the Pertusillo dam Basilicata, Italy. *Int. J. Appl. Earth Obs. Geoinf.* 52, 221–229. <http://dx.doi.org/10.1016/j.jag.2016.06.013>.
- Minissale, A., Borriani, D., Montegrossi, G., Orlando, A., Tassi, F., Vaselli, O., Huertas, A.D., et al., 2008. The Tianjin geothermal field (North-Eastern China): water chemistry and possible reservoir permeability reduction phenomena. *Geothermics* 37, 400–428. <http://dx.doi.org/10.1016/j.geothermics.2008.03.001>.
- Monserrat, O., Crosetto, M., Cuevas, M., Crippa, B., 2011. The thermal expansion component of persistent scatterer interferometry observations. *IEEE Geosci. Remote Sens. Lett.* 8 (5), 864–868. <http://dx.doi.org/10.1109/LGRS.2011.2119463>.
- Ni, Z.G., 2005. Key techniques in the fabrication process of the steel structure for Lupu Bridge. *China Railw. Sci.* 26 (6), 134–140.
- Ni, Y.Q., Hua, X.G., Wong, K.Y., Ko, J.M., Asce, F., 2007. Assessment of bridge expansion joints using long-term displacement and temperature measurement. *J. Perform. Constr. Facil.* 21 (2), 143–151. [http://dx.doi.org/10.1061/\(ASCE\)0887-3828\(2007\)21:2\(143\)](http://dx.doi.org/10.1061/(ASCE)0887-3828(2007)21:2(143)).
- Osmanoglu, B., Sunar, F., Wdowinski, S., Cabral-Cano, E., 2016. Time-series analysis of InSAR data: methods and trends. *ISPRS J. Photogramm. Remote Sens.* 115, 90–102. <http://dx.doi.org/10.1016/j.isprsjprs.2015.10.003>.
- Perissin, D., Wang, Z., Lin, H., 2012. Shanghai subway tunnels and highways monitoring through Cosmo-SkyMed persistent Scatterers. *ISPRS J. Photogramm. Remote Sens.* 73, 58–67. <http://dx.doi.org/10.1016/j.isprsjprs.2012.07.002>.
- Qin, X.Q., Liao, M.S., Yang, M.S., Zhang, L., 2017a. Monitoring structure health of urban bridges with advanced multi-temporal InSAR analysis. *Ann. GIS* 6, 1–10. <http://dx.doi.org/10.1080/19475683.2017.1382572>.
- Qin, X.Q., Liao, M.S., Zhang, L., Yang, M.S., 2017b. Structural health and stability assessment of high-speed railways via thermal dilation mapping with time-series InSAR analysis. *IEEE J. Sel. Top. Appl. Earth Observ. Remote Sens.* 10 (6), 2999–3010. <http://dx.doi.org/10.1109/JSTARS.2017.2719025>.
- Qu, F.F., Lu, Z., Zhang, Q., Bawden, G.W., Kim, J.W., Zhao, C.Y., Qu, W., 2015. Mapping ground deformation over Houston-Galveston, Texas using multi-temporal InSAR. *Remote Sens. Environ.* 169, 290–306. <http://dx.doi.org/10.1016/j.rse.2015.08.027>.
- Rucci, A., Ferretti, A., Guarnieri, A.M., Rocca, F., 2012. Sentinel 1 SAR interferometry applications: the outlook for sub millimeter measurements. *Remote Sens. Environ.* 120 (10), 156–163. <http://dx.doi.org/10.1016/j.rse.2011.09.030>.
- Shamshiri, R., Motagh, M., Baes, M., Sharifi, M.A., 2014. Deformation analysis of the lake Urmia causeway (luc) embankments in northwest Iran: insights from multi-sensor interferometry synthetic aperture radar (Insar) data and finite element modeling (fem). *J. Geod.* 88 (12), 1171–1185. <http://dx.doi.org/10.1007/s00190-014-0752-6>.
- Shi, Y.J., Yan, X.X., Chen, D.P., 2017. Engineering geological structure establishment and conditions assessment integrating land and sea in Shanghai coastal area. *Hydrogeol. Eng. Geol.* 44 (2), 96–101.
- Soergel, U., Cadario, E., Thiele, A., Thönnessen, U., 2008. Feature extraction and visualization of bridges over water from high-resolution InSAR data and one orthophoto. *IEEE J. Sel. Top. Appl. Earth Observ. Remote Sens.* 1 (2), 147–153. <http://dx.doi.org/10.1109/JSTARS.2008.2001156>.
- Sousa, J.J., Bastos, L., 2013. Multi-temporal SAR interferometry reveals acceleration of bridge sinking before collapse. *Nat. Hazards Earth Syst. Sci. Discuss.* 13 (3), 659–667. <http://dx.doi.org/10.5194/nhess-13-659-2013>.
- Teatini, P., Tosi, L., Strozzi, S., Carbognin, L., Wegmüller, U., Rizzetto, F., 2005. Mapping regional land displacements in the Venice coastland by an integrated monitoring system. *Remote Sens. Environ.* 98 (4), 403–413. <http://dx.doi.org/10.1016/j.rse.2005.08.002>.
- Torres, R., Snoeij, P., Geudtner, D., Bibby, D., Davidson, M., Attema, E., et al., 2012. GMES Sentinel-1 mission. *Remote Sens. Environ.* 120, 9–24. <http://dx.doi.org/10.1016/j.rse.2011.05.028>.
- Vilardo, G., Ventura, G., Terranova, C., Matano, F., Nardò, S., 2009. Ground deformation due to tectonic, hydrothermal, gravity, hydrogeological, and anthropic processes in the Campania region (southern Italy) from permanent scatterers synthetic aperture radar interferometry. *Remote Sens. Environ.* 113 (1), 197–212. <http://dx.doi.org/10.1016/j.rse.2008.09.007>.
- Wong, K.Y., 2004. Infrastructure and health monitoring of cable-supported bridges. *Struct. Control. Health Monit.* 11 (2), 91–124.
- Xu, Y.L., Chen, B., Ng, C.L., Wong, K.Y., Chan, W.Y., 2010. Monitoring temperature effect on a long suspension bridge. *Struct. Control. Health Monit.* 17, 632–653. <http://dx.doi.org/10.1002/stc.340>.
- Yang, M.S., Liao, M.S., Shi, X.G., Zhang, L., 2017. Land subsidence monitoring by joint estimation of multi-platform time series InSAR observations. *Geomatics Inf. Sci. Wuhan Univ.* 42 (6), 797–802. <http://dx.doi.org/10.13203/j.whugis.20140924>.
- Yarnold, M.T., 2013. Temperature-Based Structural Identification and Health Monitoring for Long-Span Bridges (Doctoral Dissertation). Drexel University.
- Yi, T.H., Li, H.N., Gu, M., 2010. Recent research and applications of GPS based technology for bridge health monitoring. *SCIENCE CHINA Technol. Sci.* 53 (10), 2597–2610. <http://dx.doi.org/10.1007/s11431-010-4076-3>.
- Zhang, X., 2000. Key construction techniques of Tianjin Rainbow Bridge. *Highway* 10, 18–22.
- Zhang, P.F., Shi, Y.J., Zeng, Z.Q., et al., 2004. Analysis and evaluation to geo-environmental conditions for the proposed site for Expo 2010 Shanghai China. *Shanghai Geol.* 4, 1–6.
- Zhang, L., Lu, Z., Ding, X.L., Jung, H., Feng, G., Lee, C., 2012. Mapping ground surface deformation using temporarily coherent point SAR interferometry: application to Los Angeles Basin. *Remote Sens. Environ.* 117 (1), 429–439. <http://dx.doi.org/10.1016/j.rse.2011.10.020>.
- Zhao, Q., Pepe, A., Gao, W., et al., 2015. A DInSAR investigation of the ground settlement time evolution of ocean-reclaimed lands in Shanghai. *IEEE Sel. Top. Appl. Earth Observ. Remote Sens.* 8 (4), 1763–1781. <http://dx.doi.org/10.1109/JSTARS.2015.2402168>.
- Zhao, J.W., Wu, J.C., Ding, X.L., Wang, M.Z., 2017. Elevation extraction and deformation monitoring by multitemporal InSAR of Lupu Bridge in Shanghai. *Remote Sens.* 9 (9), 897. <http://dx.doi.org/10.3390/rs9090897>.